# 19. Mercury's Global Evolution

**Steven A. Hauck, II** – *Department of Earth, Environmental, and Planetary Sciences, Case Western Reserve University, Cleveland, Ohio, USA (hauck@case.edu)*

**Matthias Grott** – *Department of Planetary Physics, German Aerospace Center, Berlin, Germany*

**Paul K. Byrne** – *Department of Marine, Earth, and Atmospheric Sciences, North Carolina State University, Raleigh, North Carolina, USA*

**Brett W. Denevi** – *The Johns Hopkins University Applied Physics Laboratory, Laurel, Maryland, USA*

**Sabine Stanley** – *Department of Earth and Planetary Sciences, Johns Hopkins University, Baltimore, Maryland, USA*

**Timothy J. McCoy** – *Department of Mineral Sciences, National Museum of Natural History, Smithsonian Institution, Washington, District of Columbia, USA*

**Words, including references, captions, headings, etc: 27110**

Figures: 8

## 19.1 Introduction

From formation to quiescence, the history of a planet is the consequence of an intricate set of relationships between processes that both shape the surface and operate through the entirety of the planet (Kaula, 1975). MESSENGER, which completed the first orbital investigation of Mercury in April 2015 (Chapter 1), has revealed that planet to be as rich an example of that intricacy as any of the major bodies of the inner Solar System. Mercury has long been known as a planet of enigmas, from its 3:2 spin–orbit resonance with the Sun, to its global contraction, to its unexpected magnetic field (Solomon, 2003). Now, MESSENGER has unveiled the majority of the planet that was previously unseen (Chapters 6, 9–13), characterized the large-scale chemical composition and heterogeneity of the surface (Chapters 2, 7–8), determined Mercury's shape, gravity, and rotational state (Chapters 3–4), and revealed unknown structure and ancient activity of the magnetic field (Chapter 5).

The broad set of observations of Mercury's surface and interior by MESSENGER places fundamental constraints on the processes governing the planet's evolution. Although few of these observations individually lead to unique conclusions about the history of the innermost planet, taken as a whole, and in combination with an understanding of the processes that operate on and within planets in general, they provide an important picture of how Mercury evolved. At its most basic level, a planet seen today is the consequence of how material and heat are transported on and to its surface and within the interior. Mercury's early history was marked by both intense bombardment and widespread volcanism (Chapters 6, 9, 11). Generally overprinting this record of crustal growth and reworking is a global set of tectonic features, predominantly shortening in nature and indicative of substantial contraction of Mercury, formed

largely since the end of the period of heaviest bombardment of the planet (Chapter 10). MESSENGER's observations of remanent crustal magnetism during its final year in orbit revealed that Mercury possessed an internal magnetic field early in the planet's history (Chapter 5). This result indicates that within the first several hundred million years of Mercury's history, the deep interior where the magnetic field was generated was vigorously active. Each of these findings is set against the backdrop of a geochemically diverse and quite surprising surface and, by inference, interior composition (Chapters 2, 7). Indeed, MESSENGER found Mercury to be the most chemically reduced terrestrial planet on the basis of its low surface abundance of iron and relatively large surface abundance of sulfur (Nittler *et al.*, 2011). Furthermore, MESSENGER observations showed the planet to be unexpectedly volatile rich, including considerable abundances of the heat-producing elements potassium, thorium, and uranium (Peplowski *et al.*, 2011). The chemically reduced interior has major implications for the composition of Mercury's core, its structure, and how the magnetic field is generated, as does the newly constrained understanding of the abundance of heat-producing elements, which control the rate at which the planet cooled and its ability to generate magma.

In order to better understand how Mercury evolved over the past 4.5 billion years we synthesize observations by MESSENGER that elucidate the primary processes that have governed its history. We begin by outlining results from MESSENGER that clarify both how the crust of the planet formed and the history of the crust and lithosphere, including constraints from observations of surface geochemistry, the record of volcanism and tectonics, and the structure of the crust. Then we focus on observations that provide information on the state, structure, and behavior of the deeper interior. In tandem, we investigate the thermochemical evolution of the interior of Mercury subject to the constraints provided by MESSENGER's observations. Finally,

we discuss the implications of these results for the history of the planet and outline prospects for future progress on understanding how the whole of Mercury has evolved.

## 19.2 Earliest history of the crust

### *19.2.1 Geological constraints*

The geologic record of Mercury's earliest crust – the outermost, petrologically distinct layer of the silicate portion of the planet derived from melting of the mantle (e.g., Brown and Elkins-Tanton, 2009; Namur et al., 2016; Namur and Charlier, 2017; Chapter 3) – is largely obscured by resurfacing by both impacts and volcanism (e.g., Trask and Guest, 1975; Spudis and Guest, 1988; Strom and Neukum, 1988; Denevi *et al.*, 2009). Indeed, the most heavily cratered terrain has been estimated to have an age of 4.0–4.1 Gyr (Marchi *et al.*, 2013). However, despite the fact that there are no areas of the crust that can be quantifiably ascribed to the first ~500 Myr of Mercury's history, important clues to the nature and origin of the crust are found in several areas that appear to have undergone only minimal resurfacing as well as in material exposed from depth by large impact events (Chapter 6).

Spectral units termed low-reflectance material (LRM) (Robinson *et al.*, 2008; Denevi *et al.*, 2009; Murchie *et al.*, 2015; Klima *et al*., 2016) appear to be one key to our understanding of Mercury's crust. With a reflectance of just 4–5% at 550 nm (Chapter 8), LRM is ~30% darker than Mercury's average surface and is found concentrated in the ejecta of large impact craters (Denevi *et al.*, 2009; Ernst *et al.*, 2010; Klima et al., 2016). The reflectance and spectral properties of the LRM are consistent with the deposits having a graphite component (Murchie *et al.*, 2015). Furthermore, increases in thermal neutron count rates associated with LRM deposits suggest a carbon abundance that is 1–3 wt% higher than that of surrounding terrain (Peplowski *et al.*, 2015a, 2016). These observations are consistent with the hypothesis that Mercury developed

89 a carbon-rich floatation crust due to buoyancy of graphite in an early magma ocean (Vander
90 Kaaden and McCubbin, 2015).

91 Any early crust, particularly one as thin as a graphite-rich crust might have been, was surely
92 disrupted heavily by impacts, modified by magmatic intrusions, and buried by volcanic deposits.
93 Therefore, the modern distribution of this primordial material on the surface is limited, as it has
94 been substantially mixed and diluted with other materials. By this reasoning, LRM is the
95 material with the greatest concentration of carbon in a C-rich crust (Peplowski *et al.*, 2015a). The
96 depth of origin of LRM, calculated from the excavation depth of impact craters, is often several
97 to tens of kilometers (Denevi *et al.*, 2009; Ernst *et al.*, 2010; Ernst *et al.*, 2015; Peplowski *et al.*,
98 2015a). These depth estimates provide lower bounds to the depth of burial by impact and
99 volcanic deposits subsequent to the formation of the original floatation crust. In some of the
100 most heavily cratered terrains, the overall surface is relatively low in reflectance and all impact
101 craters in the region expose LRM, suggesting that these regions may have experienced less
102 resurfacing than average (Chapter 6). However, in other large regions, no LRM is found in any
103 crater smaller than ~150 km in diameter, suggesting burial by at least 8 km of volcanic material
104 (Chapter 6). Rivera-Valentin and Barr (2014) explored impact redistribution models for an
105 impactor population consistent with Mercury's cratering record and found that the LRM is
106 consistent with a darkening agent approximately 30 km deep, which would be within the
107 lowermost crust or upper mantle (James *et al*., 2015; Padovan *et al*., 2015). Concentration of a
108 darkening agent, such as graphite, from a crustal layer deep within the crust may also imply that
109 volcanism was substantial and occurred with a flux much greater than impact redistribution of
110 upper crustal material in the period before the onset of the late heavy bombardment (LHB).

Otherwise, the darkening agent would have been efficiently mixed throughout the crust and unlikely to display variations associated with exhumation from depth.

### *19.2.2 Geochemical state of the crust and mantle*

The composition and chemical diversity of the surface of Mercury provide important insights into the nature, origin, and evolution of the crust and mantle. Given that Mercury is strongly differentiated with an uncommonly low silicate-to-metal ratio (Chapters 2, 4), understanding the mechanisms that may be responsible for Mercury's crustal formation has been a long-standing question. At their most basic, models for the formation of the crust include partial melting of an undifferentiated, chondritic-like mantle; formation as the uppermost layer of a solidifying magma ocean; or products of remelting of a magma ocean.

Geochemical observations and the relative ages of the surface units of Mercury argue against an undifferentiated mantle as the source region for melts erupted onto the surface. Melting of enstatite chondrites has been investigated experimentally and modeled from phase equilibria to understand both the origin of the highly-reduced aubrite parent body (McCoy *et al.*, 1999) and Mercury (Burbine *et al.*, 2002; Malavergne *et al.*, 2010). An undifferentiated chondritic mantle would produce sodium-rich melts at low degrees of partial melting, consistent with the composition of the northern smooth plains (NSP) (Vander Kaaden and McCubbin, 2016). However, the high Mg/Si and low Al/Si ratios observed for Mercury's average surface composition require relatively high degrees of partial melting (Burbine *et al.*, 2002; Nittler *et al.*, 2011). Further, the formation of the high-sodium flood basalts of the NSP relatively late in the history of Mercury would require a fertile mantle source that had not experienced earlier partial

133 melting. Finally, the highly differentiated nature of Mercury, including the presence of a large
134 core, argues against preservation of a wholly undifferentiated mantle.

135 A widely accepted model of the mantle and crust suggests that Mercury once had a magma
136 ocean responsible for an initial stage of silicate differentiation. Prior to MESSENGER's orbit
137 insertion and the early geochemical measurements of the surface of Mercury, the nature of the
138 crust and the bulk composition of the surface and planet were poorly constrained, although the
139 surface was known to be FeO-poor and the bulk composition of the planet rich in iron metal
140 (Taylor and Scott, 2003, and references therein). This uncertainty led to a range of magma ocean
141 models producing either a plagioclase floatation crust or a low-FeO magmatic crust, depending
142 on the bulk composition of the magma ocean (Brown and Elkins-Tanton, 2009; Riner *et al.*,
143 2009). Some of these petrologic models produce gravitationally unstable mantles that would
144 experience overturn, similar to that posited for the lunar mantle.

145 With the realization that the crust of Mercury is neither a plagioclase-rich floatation crust nor
146 chemically homogeneous, models emerged that considered a magma ocean with subsequent
147 remelting (Charlier *et al.*, 2013; Vander Kaaden and McCubbin, 2015, 2016). Charlier *et al*.
148 (2013) suggested that compositional heterogeneity observed during early MESSENGER orbital
149 observations could have been the result of melting of different layers within the mantle during
150 convection and adiabatic pressure-release melting, even in the absence of mantle overturn.
151 Vander Kaaden and McCubbin (2015) strengthened the argument against a significant primary
152 floatation crust experimentally by demonstrating that graphite is the only phase that is buoyant in
153 a Mercury magma ocean. The equivalent thickness of such a graphite layer is directly dependent
154 on the concentration of carbon in the silicate portion of the planet. Should Mercury have a bulk
155 silicate carbon content similar to those of Earth, Mars, or the Moon, that layer might be up to

~100 m thick. However, if Mercury's carbon content is more similar to that of chondritic materials, a graphite crust could range in thickness from as little as 100 m to more than 10 km, with the largest values for bulk silicate compositions similar to carbonaceous chondrites (Vander Kaaden and McCubbin, 2015). These authors further noted that, unlike many other planetary bodies, partial melts derived from mantle melting on Mercury are buoyant throughout the mantle and would rise to the surface without stalling at some neutral buoyancy depth. Thus, the crust of Mercury is likely comprised of an impact-gardened mixture of primary crust formed during a magma ocean stage and subsequent volcanic deposits. Vander Kaaden and McCubbin (2016) further refined this idea by noting that a crystallizing magma ocean without buoyant silicate phases would concentrate incompatible elements, including volatiles, near the surface of the planet. Thus, remelting of shallow cumulates can produce volatile-rich compositions, like the NSP, even at high degrees of partial melting.

## 19.3 History of the crust and lithosphere

Geological observations provide compelling evidence that Mercury's crust is largely volcanic in origin and has experienced widespread tectonic deformation. The accumulated, observable history of Mercury's crust and lithosphere contains fundamental clues to the processes that shaped the surface of the planet, and importantly, the time progression of these processes. Whereas the earliest history of the planet may have included a magma ocean and the generation of a thin and rather exotic floatation crust, it is the subsequent history that is more discernable. MESSENGER's collected geophysical, geological, and geochemical observations of Mercury provide important insights into both the planet's integrated history as well as many discrete events, of variable duration, that reflect its evolutionary path.

### *19.3.1 Crustal thickness*

In addition to the geochemical and geological markers of crustal formation, Mercury's gravity field and topography provide important clues to the nature and formation of the crust (Perry *et al.*, 2015; Tosi *et al.*, 2015; Chapter 3). Mercury's crust is the product of the combined processes of crystallization of any magma ocean and upward transport of mantle partial melts integrated over the course of the planet's history. Therefore, knowledge of the thickness of the crust is a crucial indicator of the efficiency and pattern of igneous differentiation of the planet, which in turn depend strongly on Mercury's internal activity.

Orbital observations of Mercury's gravity field by MESSENGER provided the first detailed measurements of its mass distribution. MESSENGER's eccentric orbit (Chapter 1), with the periapsis located at a high northern latitude, resulted in gravity field measurements that have the highest spatial resolution in the north and that resolve only much longer wavelengths in the southern hemisphere (Smith *et al.*, 2012; Mazarico *et al.*, 2014; Verma and Margot, 2016). Focusing on the higher-resolution information in the northern hemisphere, several estimates of the thickness of the crust have been calculated (Smith *et al.*, 2012; James *et al.*, 2015; Padovan *et al.*, 2015). The most recent of these models place the average crustal thickness of the northern hemisphere at 35 ± 18 km on the basis of geoid-to-topography ratios (GTR) (Padovan *et al.*, 2015) and place a minimum on the average thickness of 38 km with a model that accounts for both crustal and mantle sources of compensation (James *et al.*, 2015). Density differences between the crust and mantle are a major source of uncertainty in crustal thickness models. Padovan *et al*. (2015) considered a range of crustal densities from 2700 to 3100 kg $m^{-3}$, with the upper bound consistent with grain densities they inferred from MESSENGER elemental compositions, the lower bound the result of including 12% porosity throughout the crust, as has been inferred for the Moon (Wieczorek *et al.*, 2013), and a mantle density of 3300 kg $m^{-3}$. This

range overlaps independent estimates of the grain densities calculated from experimental determinations of the modal mineralogy consistent with the range of surface compositions across Mercury (Namur and Charlier, 2017). Similarly, the inversion approach of James *et al*. (2015) was for a nominal crustal density of 3200 kg $m^{-3}$ and a mantle density of 3400 kg $m^{-3}$. Generally speaking, the small difference in grain density between the crust and mantle, approximately 200 kg $m^{-3}$, is a reflection of the inferred low iron content of Mercury's silicate layers. This density difference is also important for crustal flow models, as the driving stress for any topographic relaxation via lower crustal flow scales directly with the density contrast (e.g., Nimmo and Stevenson, 2001), so a small density contrast implies less lower crustal flow. Potentially of greater importance is that the inferred crustal thickness values when compared with the thickness of the mantle imply that Mercury has experienced the most efficient extraction of crust among the terrestrial bodies. Indeed, Mercury's crust represents approximately 10% of all silicate material on the planet (James *et al.*, 2015; Padovan *et al.*, 2015). Such efficient extraction is likely the result of relatively high degrees of partial melting, consistent with geochemical observations of the surface and inferences for the interior (Chapters 2, 7).

Compared with Mercury's global shape as derived from laser altimetry and radio occultation measurements, the geoid has a spectral power of only ~1% that of the shape at spherical harmonic degree and order two, which indicates that topographic variations on Mercury at the longest wavelengths are largely isostatically compensated (Perry *et al.*, 2015). Should the variations at degree and order two be compensated by variations in the thickness of the crust, this difference would imply a ~24 km pole-to-equator change in crustal thickness. However, other mechanisms such as variations in density due to temperature or composition may contribute to the compensation, potentially reducing any long-wavelength crustal thickness variation (Perry *et*

225 *al.*, 2015; Tosi *et al.*, 2015; Chapter 3). Regardless, a substantial latitudinal variation in the
226 crustal thickness of Mercury would be an important, if as yet poorly understood, constraint on
227 crustal production (Chapter 3).
228
229 ***19.3.2 Surface history***
230 One of the more direct measures of the evolution of a planet's crust is the geological history
231 of its surface. To first order, Mercury's surface can be classified into units of either smooth
232 plains or intercrater plains (Chapter 6). The former type of unit is texturally smooth and
233 relatively sparsely cratered, displays sharp boundaries with adjacent regions, and is level to
234 gently sloped over baselines of ~100–200 km (Trask and Guest, 1975; Denevi *et al.*, 2013a;
235 Chapter 6). These smooth plains units occupy about 27% of the planet's surface (Figure 19.1)
236 and are predominantly located in the northern hemisphere in the NSP and within and adjacent to
237 the Caloris basin. The remainder of the surface is largely dominated by intercrater plains, which
238 are characterized by gently rolling terrain with gradational boundaries and a greater density of
239 secondary craters 5–10 km in diameter than smooth plains (Trask and Guest, 1975; Denevi *et al.*,
240 2013a). The intercrater plains are situated between individual and clusters of large (>30 km)
241 craters, which generally superpose the plains and are the source of the secondary craters. As the
242 density of superposed impact craters appears to be the main distinction between the varieties of
243 plains (Byrne *et al*., 2016), their main difference likely reflects a range in age rather than specific
244 lithological or rheological differences (Murray *et al.*, 1975; Strom, 1977; Spudis and Guest,
245 1988; Denevi *et al.*, 2009; Whitten *et al.*, 2014). Little evidence remains of an older, more
246 heavily cratered surface apart from several regions that have undergone only partial resurfacing
247 or portions of basin massifs that predate the intercrater plains (Chapter 6).

Observations of Mercury have established that the planet has been heavily shaped by volcanic activity. For example, the majority of smooth plains units are interpreted as effusive volcanic deposits, on the basis of their distinct unit boundaries, embayment relations with surrounding topography, the presence of buried "ghost craters" within these units, spectral differences with neighboring terrain, and deposits located far from any large basins (Murray *et al.*, 1974, 1975; Strom *et al.*, 1975; Spudis and Guest, 1988; Robinson and Lucey, 1997; Head *et al.*, 2008, 2011; Murchie *et al.*, 2008; Robinson *et al.*, 2008; Denevi *et al.*, 2009, 2013a; Chapter 11). A number of other volcanic landforms formed by effusive activity have also been reported across the planet, including a small shield volcano, lobate flow margins, and lava-sculpted valles (Head *et al.*, 2008, 2011; Byrne *et al.*, 2013; Hurwitz *et al.*, 2013). Landforms attributed to explosive volcanism (e.g., Kerber *et al.*, 2009; Thomas *et al.*, 2014), often in close spatial proximity to smooth plains, have also been identified.

The major smooth plains deposits on Mercury have crater densities that vary by up to a factor of 5 for craters larger than 10 km. However, because of the inferred rapid decline in cratering during their formation, their derived model ages are the same, within statistical error, for any of the published model production function (MPF) chronologies for Mercury (Strom and Neukum, 1988; Neukum *et al.*, 2001; Marchi *et al.*, 2009; Le Feuvre and Wieczorek, 2011), though differences among the model chronologies are greater for lower-density (younger) deposits (Chapter 9). Crater size–frequency analyses have shown that the NSP, the single largest smooth plains deposit on the planet (Chapter 6), as well as the plains interior to the Caloris and the Rembrandt impact basins, were emplaced around 3.7–3.8 Ga (Fassett *et al.*, 2009; Head *et al.*, 2011; Strom *et al.*, 2011; Denevi *et al.*, 2013a; Ferrari *et al.*, 2014; Ostrach *et al.*, 2015; Chapter 9). The areal densities of impact craters for two additional large smooth plains deposits on

Mercury, those near the Faulkner crater and the Rachmaninoff basin, are comparable to the densities for the NSP and Caloris interior plains (Fassett *et al.*, 2009; Denevi *et al.*, 2013a; Whitten *et al.*, 2014; Ostrach *et al.*, 2015), implying that these other units are similar in age. Crater density measurements for several additional, smaller smooth plains deposits yield ages of ~3.8–3.5 Ga for these sites (Byrne *et al.*, 2016) with the crater model production function of Le Feuvre and Wieczorek (2011). Only one definitively volcanic smooth plains deposit has been identified on the planet with a substantially younger age than those above. Situated within the inner peak ring of the Rachmaninoff impact basin, this deposit is considerably smaller than other plains units for which ages have been determined (Prockter *et al.*, 2010; Marchi *et al.*, 2011). The distribution of the model ages of smooth plains units (in particular the units shaded dark purple in Figure 19.1), which are stratigraphically the youngest effusive volcanic features on Mercury, suggest therefore that flood volcanism was largely completed by ~3.5 Ga (Byrne *et al*., 2016).

Similar to the smooth plains, intercrater plains units have a range of crater areal densities, the lowest values of which overlap the highest corresponding values for smooth plains units (Whitten *et al.*, 2014; Byrne *et al.*, 2016). The model ages of the intercrater plains are ~3.9–4.1 Ga (e.g., Whitten *et al.*, 2014; Chapter 9). Notably, nowhere on Mercury is as heavily cratered as the lunar highlands (Strom, 1977; Strom *et al.*, 2008; Fassett *et al.*, 2011; Marchi *et al.*, 2011), and the most heavily cratered regions on Mercury have been dated at just 4.0–4.1 Ga (Marchi *et al.*, 2013) with the chronology of Marchi *et al*. (2009). These model age results suggest that little remains of the geologic record of the earliest ~500 Myr of Mercury's surface history (Chapters 6, 9).

293 The origin of Mercury's intercrater plains is less certain than that of the smooth plains, but
294 they may also be dominantly products of volcanism. The main line of evidence lies in their age:
295 model ages of 4.0–4.1 Ga require major resurfacing of the earliest crust, with volcanism being a
296 likely major cause (Head *et al.*, 2011; Denevi *et al.*, 2013a; Whitten *et al.*, 2014; Chapters 6, 11).
297 For example, Whitten *et al*. (2014) showed that cratering of smooth plains, particularly by
298 secondaries from nearby primary craters, renders those smooth deposits texturally similar to
299 intercrater plains. Large regions within the intercrater plains have also been interpreted as
300 volcanic in origin on the basis of a substantial deficit of the most degraded class of craters, as
301 well as stratigraphic and color relationships that are analogous to volcanic smooth plains deposits
302 (Denevi *et al.*, 2013b; Chapter 6). Although discrete volcanic landforms may not have survived
303 the history of impact bombardment of Mercury prior to the emplacement of the smooth plains,
304 thermochemical evolution models of the planet imply that voluminous and widespread effusive
305 volcanic activity operated for at least the planet's first half-billion years (Michel *et al.*, 2013;
306 Tosi *et al.*, 2013). If so, then the intercrater plains we observe today are likely just older smooth
307 plains deposits (e.g., Strom, 1977; Spudis and Guest, 1988; Denevi *et al.*, 2009; Whitten *et al.*,
308 2014). This inference is consistent with the observed compositional heterogeneity on Mercury,
309 where differences in composition do not always follow morphologic boundaries, and where
310 smooth and intercrater plains can share similar compositions (Weider *et al.*, 2015).
311 The cessation of large-scale effusive volcanism on Mercury, as seen in the smooth plains and
312 the older intercrater plains, effectively heralded the end of the crust-building phase of Mercury's
313 evolution, but volcanic activity in some form continued thereafter. For example, the
314 identification of irregular pits across Mercury, often characterized by a lack of a raised rim,
315 scalloped edges, and diffuse-edged deposits with a distinct reddish color, provides evidence for

316 explosive volcanism having occurred on the planet (Head *et al.*, 2008; Murchie *et al.*, 2008;
317 Kerber *et al.*, 2009; Chapter 11). Some of these pyroclastic deposits may be as young as ~1 Ga
318 (Thomas *et al.*, 2014). Many of Mercury's explosive volcanic landforms and deposits are
319 spatially associated with areas of pre-existing crustal weaknesses, including the surface breaks of
320 thrust faults underlying lobate scarps and within the heavily fractured central peaks and peak
321 rings of craters (Figure 1) (Kerber *et al.*, 2011; Thomas *et al.*, 2014; Chapter 10). Additionally,
322 the areal extents of pyroclastic deposits are far less than those of effusive volcanic deposits.
323 Although widely distributed, the role of explosive volcanism in the building and resurfacing of
324 Mercury's crust was negligible compared with the contribution from effusive volcanism.

325 The history of Mercury's surface is recorded as much in its tectonic landforms as in its
326 volcanic ones. Indeed, the surface of Mercury is replete with tectonic features, including
327 landforms termed "wrinkle ridges" and "lobate scarps" (see the bottom panel of Figure 1),
328 interpreted to have accommodated crustal shortening in response to global contraction (Strom *et*
329 *al.*, 1975). The number and structural relief of this ensemble of landforms correspond to a
330 decrease in planetary radius of at least 5 to 7 km (Byrne *et al.*, 2014; Chapter 10). These figures
331 are in stark contrast with earlier estimates from more limited Mariner 10 data and early flyby
332 data from MESSENGER that suggested that perhaps no more than 2 km of contraction was
333 likely (Strom *et al.*, 1975; Watters *et al.*, 1998, 2009). Importantly, crater and thrust fault
334 superposition relations indicate that global contraction was underway by around the time that
335 widespread effusive volcanism came to an end (Banks *et al.*, 2015; Byrne *et al*., 2016).
336 Observations of craters formed during the Calorian system (Spudis and Guest, 1988; Chapter 9)
337 that superpose scarps show that shortening of Mercury's surface on at least a regional scale had
338 begun at some time before ~3.6 Ga (Banks *et al.*, 2015). Further, the discovery with

MESSENGER low-altitude image data of a population of lobate scarps at least an order of magnitude smaller than previously recognized (Watters *et al.*, 2015b), and the stratigraphic relationships between such scarps and impact craters with a range of degradation states, is suggestive that tectonic accommodation of global contraction persisted over most of Mercury's history (Banks *et al.*, 2015).

Observations made with MESSENGER data have helped characterize the resurfacing mechanisms and history of the innermost planet. Voluminous magma genesis within Mercury's interior likely resulted in globally extensive effusive volcanism that persisted for at least several hundred million years. This volcanic activity, together with an increase in the impact flux at the start of the LHB, has obscured the geological record of the first ~500 Myr of Mercury's surface history. With a reduction in magma genesis as a result of secular cooling and with the horizontal compressive state in Mercury's lithosphere resulting from global contraction, widespread effusive volcanism began to wane, with eruptive volumes decreasing with time, before ultimately ending by about 3.5 Ga. Explosive volcanism endured for far longer, but the vast majority of Mercury's crust was in place prior to 4 Ga, and smooth plains formation constituted the tapering end of the planet's crust-building phase.

### *19.3.3 Chemical and petrological constraints on crustal formation*

Observations by MESSENGER's suite of geochemical sensors have provided important insight into the composition of the planet, the make-up of the crust, and how it formed (Chapters 2, 7). In particular, the X-Ray Spectrometer (XRS), Gamma-Ray Spectrometer (GRS), and Neutron Spectrometer (NS) provided spatially resolved surface abundances of U, K, and Th, as well as Si-normalized elemental abundances for Na, Mg, Al, S, Cl, Ca, Ti, Cr, Mn, Fe, and O. On a global scale, XRS measurements (Nittler *et al.*, 2011) indicate that the surface of Mercury

362 exhibits a high Mg/Si ratio (0.33–0.67), which is intermediate between those of terrestrial
363 oceanic and lunar mare basalts and highly magnesian komatiites. Mercury's surface also
364 exhibits lower Al/Si and Ca/Si ratios than typical terrestrial or lunar basalts. Most surprising,
365 high S/Si ratios (0.05–0.15) suggest abundances of the moderately volatile element S up to ~4 wt
366 %. Observations from the GRS further argue against a volatile-depleted composition for
367 Mercury. For example, Mercury's K/Th ratio is comparable with that of other terrestrial planets
368 and is much higher than observed in the volatile-depleted lunar crust (Peplowski *et al.*, 2011).
369 Moreover, large ratios of Na/Si (0.12) and Cl/Si (0.0057) are also observed (Evans *et al.*, 2012,
370 2015). Together, these observations suggest a magnesium-rich, iron-poor crust formed under
371 chemically reducing conditions, yet not depleted in volatiles as had been predicted for an iron-
372 rich planet so close to the Sun (e.g., Taylor and Scott, 2003).

373 The surface of Mercury exhibits considerable chemical and, therefore by extension,
374 mineralogical diversity. This diversity is best documented in the northern hemisphere, where
375 high-spatial-resolution measurements allow us to distinguish discrete geochemical terranes
376 (Chapters 2, 7). These include the northern geochemical terrane, the Caloris interior plains
377 terrane, the high-magnesium terrane, and the "low fast" terrane (so named because it has a low
378 count rate for fast neutrons). Among these terranes, the northern geochemical terrane and the
379 low fast terrane are present largely, though not exclusively, within the northern smooth plains.
380 The Caloris interior plains terrane corresponds spatially to the boundaries of the smooth plains
381 within the Caloris impact basin. In contrast, the high-magnesium terrane is geochemically
382 coherent in a number of features but exhibits no clear correlation with spectral or morphometric
383 features across the entirety of the region. However, while the crustal thickness within the
384 majority of the region is similar to the average of the northern hemisphere, the northern and

eastern boundaries are approximately coincident with areas that transition from average to thicker-than-average crust (Chapter 3). In contrast to the well-resolved XRS measurements in the northern hemisphere, the large XRS footprints in the southern hemisphere yield only a single hemispheric average composition.

Chemical compositions derived from the four distinct, northern-hemisphere geochemical terranes range in composition from basaltic andesite to trachyte on the basis of their total alkali content (Na and K) compared with silica, but ultimately all share a boninite classification due to their high MgO (> 8 wt %) and low $TiO_2$ (<0.5 wt %) concentrations. A common feature of all these geochemical terranes is that each has high volatile element concentrations, with Na ranging from 2.6 to 5.7 wt % and S from 1.8 to 2.9 wt %. Considerable geochemical differences do exist between the terranes, particularly with respect to Na, Mg, Al, and Fe, all of which differ by factors of 1.8 or greater among the terranes. The low fast terrane is most similar to the average surface composition for the planet. However, it is geochemically distinct from the northern geochemical terrane, with the two terranes combined occupying much of the NSP. Mineralogically, these terranes share the common feature of being unusually rich in normative plagioclase (37–58 wt %) (see Chapter 7). If classified as plutonic igneous rocks, these terranes would include norite, anorthositic norite, and anorthositic gabbro, reflecting differences in plagioclase abundance and the ratio of high-calcium to low-calcium pyroxene. The high-magnesium terrane is distinctive in its unusually high concentration of normative olivine (31 wt %).

### *19.3.4 Evolution of the lithosphere*

408 The mechanical behavior of the lithosphere – the outer portion of the planet that behaves as a
409 mechanically strong layer and includes portions of the crust and possibly mantle – provides key
410 insights into the history of planetary stresses and temperatures. This behavior is recorded in both
411 the tectonic landforms the lithosphere hosts (e.g., Chapter 10) and in the flexural response to
412 loads inferred from gravity and topography data (e.g., Chapter 3). For example, elastic
413 dislocation modeling of topographic profiles derived from Mariner 10 stereophotogrammetric
414 data of select lobate scarp features indicates that the underlying faults penetrate, and thus the
415 lithosphere deformed in a brittle fashion, to depths of 25–30 km, at the time of faulting (e.g.,
416 Watters and Nimmo, 2010). A comprehensive assessment of the spatial variation in lithospheric
417 thickness from this or similar techniques, however, has yet to be completed. Interestingly, this
418 estimate of the depth to the brittle–ductile transition from lobate scarp fault depths is consistent
419 with models of lithospheric strength for time periods prior to ~3.5 Ga (Williams *et al.*, 2011).
420 At regional and more local scales, stresses in the lithosphere can be modified by loads
421 produced by volcanism and impact basin formation and evolution (e.g., Kennedy *et al.*, 2008;
422 Freed *et al.*, 2009; Blair *et al.*, 2013). Nonetheless, the history of the state of stress in Mercury's
423 lithosphere has been dominated by some combination of two independent, globally acting
424 processes: despinning from a likely early, rapid rate of rotation, and global changes in planetary
425 radius arising from internal temperature changes (and cooling in particular) (Chapter 10). During
426 planetary spin-down, an equatorial bulge supported by the planet's lithosphere would have
427 relaxed (Melosh, 1977), forming a global set of near-surface joints with no preferred orientation
428 at the poles but with an increasingly prominent east–west fabric toward the equator, under the
429 assumption of a globally uniform lithospheric thickness (Klimczak, 2015). Similarly, also under
430 the assumption of globally uniform lithospheric properties, a reduction in planetary volume from

cooling of the core and mantle and from mineralogical phase changes (e.g., core crystallization) would yield a stress state in which horizontal compressive stresses exceed vertical stresses and under which a global set of thrust faults with no preferred orientation would develop (Melosh and McKinnon, 1988). However, spatial variations in lithospheric thickness, such as those imparted by long-lived latitudinal and longitudinal differences in surface temperature (Williams *et al.*, 2011; Tosi *et al.*, 2015), may further have influenced how tectonic deformation on Mercury was exhibited (Beuthe, 2010). Furthermore, the combination of stresses from both despinning and global contraction may have had a substantial influence on the stress state and the style of brittle tectonic deformation at the surface of the planet (Melosh and Dzurisin, 1978; Dombard and Hauck, 2008; Beuthe, 2010). Reorientation as a result of true polar wander, for example, driven by the formation of a large load such as the Caloris basin (Matsuyama and Nimmo, 2009), could also have altered the prevailing stress state.

Global mapping of Mercury's tectonic landforms from MESSENGER image data (Byrne *et al.*, 2014; Watters *et al.*, 2015a) has not revealed, to first order, any evidence of planet-wide, organized patterns of tectonic landforms predicted by earlier studies of despinning (e.g., Melosh, 1977; Melosh and McKinnon, 1988; Matsuyama and Nimmo, 2009; Beuthe, 2010). Given Mercury's near-zero obliquity, solar illumination at the equator is always due east or due west, which facilitates the identification of tectonic landforms that strike ~north–south (Byrne *et al.*, 2014) more easily than those trending east–west at low to mid latitudes. Landforms between 60°S and 60°N, in particular, show a predominantly north–south orientation. Landforms north of 60°N show some clustering at southwest–northeast trends but are not as strongly oriented as those at mid- to low latitudes; landforms south of 60°S show no preferred orientations (Byrne *et al.*, 2014). Nonetheless, when the effect of solar azimuthal illumination is considered, a general

~north–south trend for mid- to low-latitude landforms remains (Watters *et al.*, 2015a). Under the assumption that currently published tectonic maps are generally complete and that no bias in lighting geometry has obscured substantial ~east–west-tending landforms yet to be identified (Chapter 10), the history of stress within Mercury's lithosphere must be reconciled with these observations.

The lack of opening-mode fractures on Mercury, aside from those identified within volcanically flooded impact features (Freed *et al.*, 2012; Klimczak *et al.*, 2012; Chapter 10), indicates that no direct evidence of tidal despinning alone remains. Given that tidal despinning likely occurred geologically rapidly – although the timing of this process remains to be characterized fully – it is perhaps no surprise that such evidence is missing from the geological record, especially given that the oldest terrain on Mercury is ~4.1 Ga (section 19.3.2). On the other hand, shortening structures on the innermost planet do not form a globally heterogeneous pattern, the expected result of global contraction alone.

It may be, then, that the most straightforward interpretation of the global pattern of orientations of Mercury's tectonic landforms represents some combination of despinning and global contraction (Klimczak, 2015; Chapter 10). Thrust faults developing in such a stress state would have developed with preferred north–south orientations near the equator (Klimczak, 2015), though the expected pattern near the poles could be oriented either somewhat randomly (Klimczak, 2015), depending on rock strength, or might have a more organized pattern if latitudinal variations in lithospheric thickness were substantial (Beuthe, 2010). Regardless, this general pattern in the mid-latitudes with a differing orientation at high-latitudes is similar to that observed from global mapping (Byrne *et al.*, 2014). As such, it indicates that either tidal despinning temporally overlapped with global contraction, or that despinning imparted some

477 fabric to Mercury's lithosphere that survived until the onset of, and influenced the tectonic
478 deformation from, global contraction. The lack of a clear signature of reorientation stresses as
479 would be reflected in an orientation of the lobate scarp structures (Matsuyama and Nimmo,
480 2009) suggests that true polar wander was not a major component of the processes that drove
481 tectonic deformation. Thus, the relative timing of global contraction and despinning, as well as
482 the effects of spatial variations in lithospheric thickness (e.g., Beuthe, 2010) when considered
483 with possible values for the degree of lithospheric fracturing (e.g., Klimczak, 2015), are
484 important questions that remain outstanding.
485

486 **19.4 Knowledge of the interior**

487 ***19.4.1 Constraints on core composition***

488 Observations of low ferrous iron concentrations and larger-than-expected sulfur abundances
489 on Mercury's surface indicate that the planet's surface and, by extension, interior are strongly
490 chemically reduced (Nittler *et al.*, 2011; Weider *et al.*, 2012; Chapter 2). Inferred oxygen
491 fugacities range between 3 and 7.3 $\log_{10}$ units below the iron–wüstite (IW) buffer, with a
492 consistent overlap between published estimates of IW-4.5 to IW-6.3 (Malavergne *et al.*, 2010;
493 McCubbin *et al.*, 2012; Zolotov *et al.*, 2013). Under these highly reducing conditions, elements
494 that are normally lithophile and incorporated into silicates and oxides can instead have
495 chalcophile or siderophile behavior, combining to form sulfides or metallic phases. This
496 behavior is observed in aubrite meteorites, which formed at similarly reducing conditions and
497 contain a host of exotic sulfides, metals, carbides, phosphides, and nitrides (Keil, 1989). For the
498 surface of Mercury, correlated S/Si and Ca/Si abundances have been invoked to postulate the
499 presence of oldhamite (CaS) (Nittler *et al.*, 2011), although more recent studies (Stockstill-Cahill

500 *et al.*, 2012; Vander Kaaden and McCubbin, 2016; Vander Kaaden et al., 2016) favor complex
501 sulfides of Fe, Mg, Ti, Cr, and Mn, as well as Ca.

502 Although Fe and Ni are expected to be primary components of Mercury's core, the highly
503 reducing conditions inferred from surface materials, if indicative of conditions in Mercury's
504 interior, will also have led to the incorporation of light elements into the core, most notably Si
505 and S. As conditions become more reducing, Si becomes more soluble in the metal phase (e.g.,
506 Berthet *et al.*, 2009; Malavergne *et al.*, 2010; Chabot *et al.*, 2014). A similar trend is also
507 observed as temperatures increase (McCoy *et al.*, 1999). During planetary differentiation, Si can
508 be incorporated into the metallic phase and thus into the core of a planetary body. In practice,
509 the segregated core material under reducing conditions contains S as well, so that the Fe–S–Si
510 system rather than the binary Fe–Si system governs phase relations. Within the Fe–S–Si system
511 (Raghavan, 1988), liquid immiscibility can occur, producing separate S-rich and Si-rich metallic
512 liquids. Chabot *et al*. (2014) noted this behavior in experiments in which Fe–S–Si liquids
513 occurred in equilibrium with silicate melts for which the sulfur concentration was comparable
514 with that observed on the surface of Mercury (1–4 wt % S). These authors noted that, whereas
515 the co-existing Fe–S–Si melts (and, by extension, the core of Mercury) can readily contain both
516 sulfur and silicon, changing oxygen fugacity may result in either high-Si, low-S or high-S, low-
517 Si melts, either of which could satisfy the constraint imposed by the presence of sulfur-rich
518 silicate melts on the surface of Mercury.

519 Additional, less well-constrained light elements that might be incorporated into the core are C
520 and P. The inference that graphite could both crystallize from and occur as a floatation product in
521 an early Mercury magma ocean (Vander Kaaden and McCubbin, 2015) suggests that Mercury's
522 core might be saturated in carbon if the mantle and core were in equilibrium, as carbon tends to

be siderophile at reducing conditions. Although likely a minor constituent in Mercury's core, it may have a substantial effect on its melting behavior (Deng *et al.*, 2013a; Martin *et al.*, 2014; Martin *et al.*, 2015). Phosphorus also behaves as a siderophile under reducing conditions, forming Fe,Ni-phosphides. No measurement of phosphorus on the surface of Mercury yet exists, although its incorporation into the core in minor concentrations would be expected, potentially resulting in a complex behavior of the core governed by the Fe–S–Si–C–P system.

### *19.4.2 Internal structure*

Planetary evolution is intimately intertwined with the distribution of materials within the interior of the body. The processes of metal–silicate differentiation, core crystallization, mantle convection, and magmatism tend to result in a layered compositional and density structure within the interior of a planet. Such a layered structure is typically comprised of one or more Fe-rich layers in the planet's core, as well as one or more silicate mantle layers, all topped by a silicate crust. The thickness, material properties, and heat-producing element content of each of these layers controls how the planet generates and loses heat, generates magma, and produces a magnetic field – although neither of the latter two is guaranteed.

Mercury's large bulk density of ~5430 km $m^{-3}$ has long been understood to imply that the planet has an unusually large metal-to-silicate ratio (Siegfried and Solomon, 1974; Solomon, 1976). Consequently, Mercury has a relatively large metallic core with a comparatively thin layer of overlying silicate material. Mariner 10's discovery of Mercury's magnetic field (Ness *et al.*, 1975) suggested the possibility that the core could be partially molten. The presence of a liquid layer within the core was subsequently confirmed by Earth-based radar observations of the libration and orientation of Mercury (Margot *et al.*, 2007; Chapter 4). Pre-MESSENGER studies also used the long-wavelength gravity field to estimate the thickness of the planet's crust

546 (Anderson *et al.*, 1996) at ~100–300 km. Such a large crustal thickness was exceptionally
547 surprising because it represented one-sixth to one-half of the estimated silicate content of the
548 planet, far in excess of that for any other known planetary body. Constrained only by the radius
549 and bulk density of the planet, the relative size of Mercury's core, and whether it contained a
550 solid inner core, remained similarly uncertain. However, in models of Mercury's internal
551 evolution it was commonly assumed that the silicate portion of the planet was ~600 km thick
552 with the remainder of the interior comprised of an Fe-rich core (e.g., Schubert *et al.*, 1988;
553 Hauck *et al.*, 2004; Redmond and King, 2007; Grott *et al.*, 2011).

554 Measurements of Mercury's gravity field by the MESSENGER spacecraft have led to greatly
555 improved estimates of the planet's internal structure (Smith *et al.*, 2012; Hauck *et al.*, 2013;
556 Rivoldini and Van Hoolst, 2013; Chapter 4). That Mercury occupies a Cassini state, wherein the
557 rotation axis is approximately perpendicular to the plane of its orbit about the Sun and the spin
558 and precession rates of the planet are equal, presents an opportunity to estimate the planet's
559 structure. Indeed, a procedure was developed to determine the normalized polar moment of
560 inertia and the fraction of that moment contributed by the outermost solid portion of the planet
561 (e.g., Peale, 1988; Peale *et al.*, 2002) as a result of Mercury's special rotation state. The
562 background and details of this experiment and its interpretation are discussed at length in
563 Chapter 4. The fundamental result is that through measurement of just four quantities – the polar
564 and equatorial oblateness of the gravity field expressed as the second-degree spherical harmonic
565 coefficients $C_{20}$ and $C_{22}$, the amplitude of the physical libration, and the obliquity of the planet –
566 it is possible to resolve two measures of the radial density distribution of the planet (Peale, 1988;
567 Peale *et al.*, 2002; Margot *et al.*, 2007; Margot *et al.*, 2012; Chapter 4). These quantities are the

568 normalized polar moment of inertia $C/MR^2$ and the fraction of the polar moment of inertia
569 contributed by the portion of the planet that overlies the liquid outer core $C_m/C$.

570 The MESSENGER-derived moment of inertia values and the bulk density of the planet have
571 been used to constrain the relative thicknesses of the silicate mantle and metallic core, and their
572 respective densities, in suites of models of varying complexity (Margot *et al.*, 2012; Hauck *et al.*,
573 2013; Rivoldini and Van Hoolst, 2013; Dumberry and Rivoldini, 2015; Chapter 4). Early
574 estimates for the average density of the outermost solid layer of the planet and the metallic core
575 of 3380 ± 200 kg $m^{-3}$ and 6980 ± 280 kg $m^{-3}$, where the boundary between these two layers is
576 ~420 ± 30 km below the planet's surface (Hauck *et al.*, 2013), are consistent with the most recent
577 estimates of Mercury's gravity field and rotational parameters (Mazarico *et al.*, 2014) because of
578 the similarity to previous estimates of these parameters (Margot *et al.*, 2012).

579 Detailed models of Mercury's interior have been designed to resolve additional layers within
580 the interior. For example, as discussed in section 19.3.1, detailed analyses of gravity and
581 topography data returned by MESSENGER have led to improved estimates of the thickness of
582 the silicate crust of 35 ± 18 km or >38 km, depending on the method employed (James *et al.*,
583 2015; Padovan *et al.*, 2015; Chapter 3). That the average density of the outermost solid shell of
584 the planet is greater than expected for iron-poor silicate materials, together with estimates of the
585 composition of Mercury's core inferred from the strongly chemically reducing conditions
586 discovered at the surface, have led to the consideration of a solid iron sulfide layer at the top of
587 the core (Smith *et al.*, 2012; Hauck *et al.*, 2013; Padovan *et al.*, 2014; Chapter 4). Given that
588 both silicon and sulfur should have partitioned into the core (Chapter 2; Section 19.4.1), at the
589 modest pressures prevalent at the top of the core, melting Fe–S–Si can yield two immiscible
590 liquids (one Fe–S rich and the other Fe–Si rich) over a broad range of bulk compositions. This

591 behavior would lead to segregation of the sulfur-bearing liquids to the shallowest portions of the
592 liquid core, including the core–mantle boundary. Recent metal–silicate partitioning experiments
593 at 100 kPa (1 bar) pressure, however, suggest that the range of potential core sulfur and silicon
594 contents consistent with the surface S content may not lead to core compositions that permit
595 immiscibility and compositional segregation (Chabot *et al.*, 2014) (see also Chapter 4).
596 Additional experimental work at higher pressures and varying silicate compositions are
597 necessary to fully test the importance of liquid immiscibility in Mercury's core and the
598 possibility of a solid FeS layer. However, measurement of induced magnetic fields at Mercury
599 has led to estimates of the depth to the top of the core (Johnson *et al*., 2016; Chapter 5) that are
600 consistent with internal structure models. Taken together, the consistency between the internal
601 structure models that give an estimate of the depth to the top of the liquid outer core, and the
602 induced magnetic field analyses that yield the depth to the top of an electrically conducting layer,
603 indicates that any FeS layer, if present, is limited in thickness.
604 Similarly, an Fe-rich solid inner core may also be present, though constraints on its size are
605 sparse. Internal structure models consistent with the gravity field and rotational state of Mercury
606 are generally limited in their ability to resolve the inner core (Chapter 4), though there does
607 appear to be a slight tendency toward relatively modest inner core sizes (Hauck *et al.*, 2013;
608 Dumberry and Rivoldini, 2015), perhaps smaller than half the total core radius. Recent work on
609 the dynamic coupling of the rotation of the inner core to the outer, librating solid shell of the
610 planet indicates that for inner cores larger than ~30% of the radius of the planet, it is necessary to
611 know the size of the inner core in addition to the gravity field and rotation data in order to infer
612 the moments of inertia of the planet (Peale *et al.*, 2016; Chapter 4). Although at present it is not
613 possible to determine independently the size of the inner core, models with inner cores larger

than 30% of the radius of the planet tend to have silicate layer densities less than the densities of magnesian olivine and pyroxene, the likely dominant constituents of Mercury's mantle. Thus, Mercury's inner core, if present, is unlikely to have a radius more than 30% of the planet's radius.

### *19.4.3 Magnetic field*

Mercury's magnetic field observations demonstrate that a global-scale field is presently being generated by a core dynamo (Chapter 5). Initial data from Mariner 10, along with the more recent MESSENGER mission measurements, show that Mercury's dynamo-generated field is relatively weak and dominated by an axially aligned dipole. The dipole dominance of the field suggests, at first glance, that Mercury's dynamo may be quite Earth-like in its morphology, although a suite of characteristics of Mercury's field suggest that it has distinctive properties.

The weak intensity of the field challenges our understanding of how Mercury's magnetic field is generated. Both energy- and force-balance arguments suggest that Mercury's observed magnetic field should be at least two orders of magnitude stronger than the field measured by Mariner 10 and MESSENGER. Although the dipole is the largest harmonic in the field, the quadrupole component is relatively large, at approximately 40% of the dipole strength. This quadrupolar component – equivalent to an offset of the dipole from Mercury's center – is larger than observed for other planets with dipole-dominated fields. Indeed, it is larger than those of other planets even when corrections are made for the relatively shorter distance from the surface to the core–mantle boundary (CMB) at Mercury, with a proportionately smaller attenuation of the quadrupole component with distance from the dynamo region. The multipolar terms beyond the quadrupole, though, are quite small. Furthermore, a property that has not received much attention to date is the axisymmetry of the dipole and quadrupole components. With the possible

637 exception of Saturn, no other planet has a field as axisymmetric as Mercury. The combination of
638 these three characteristics requires alterations to dynamo scenarios previously proposed for
639 Mercury.

640 The weakness of Mercury's field was the first puzzle to be confronted, and several solutions
641 have been suggested (e.g., Wicht and Heyner, 2014). For example, numerical dynamo models
642 with very large inner cores (Stanley *et al.*, 2005) or with very small inner cores (Heimpel *et al.*,
643 2005) could produce relatively weak fields. However, current compositional, thermal, and
644 structural models for Mercury's core suggest that the inner core is unlikely to be sufficiently
645 large to satisfy the large inner core models, even if the size of the inner core is weakly
646 constrained at best (see section 19.4.2). Another explanation for the relative weakness of
647 Mercury's field is that the outer portion of the core may be stably stratified, an idea consistent
648 with the small magnitudes of the terms beyond the quadrupole in the field's multipolar
649 expansion. This stratification could be thermal (the result of subadiabatic heat flux at the CMB)
650 or compositional (due to light element segregation) in origin. Such a stably stratified layer may
651 attenuate the field intensity observed at the surface (Christensen, 2006; Christensen and Wicht,
652 2008), although double-diffusive convection in the stable layer may hinder the attenuation
653 (Manglik *et al.*, 2010). A third suggestion is that feedback between currents generated in
654 Mercury's magnetosphere and those in Mercury's core may result in a weak field state
655 (Glassmeier *et al.*, 2007; Heyner *et al.*, 2011). A fourth possibility is that, if S is the principal
656 light element in the core, temperatures may drop below the melting temperature near the top and
657 the middle of the core in regions often termed Fe-snow zones, where Fe would crystallize and
658 then sink through the core; this situation contrasts with that of Earth, where crystallization first
659 occurs at the center of the planet (Chen et al., 2008). A proposed consequence of such top-down

660 crystallization in Mercury's core is that there could be two separate regions of dynamo
661 generation and that the dipole components oppose each other, yielding a weak net external field
662 (Vilim *et al.*, 2010).

663 Although these scenarios offer promising avenues for understanding the weakness of
664 Mercury's field, they must also explain the other characteristics of the magnetic field observed
665 by MESSENGER. None of these proposed mechanisms, by themselves, have yet been shown to
666 naturally lead to magnetic fields with large quadrupole components and very axisymmetric
667 fields. The combination of a large quadrupole component and an axisymmetric dipole
668 component is particularly challenging because dynamo theory demonstrates that when a fluid
669 velocity mode excites the generation of the axial quadrupole component, it will also excite the
670 non-axisymmetric dipole component (Bullard and Gellman, 1954). Special circumstances may
671 therefore apply in order to dampen only one of these magnetic modes.

672 Two recent studies have had some success in this vein. Cao *et al*. (2014) imposed a north–
673 south symmetric thermal perturbation at the CMB in a numerical dynamo model (resulting in
674 higher heat flux at the CMB equator: see Figure 19.3) along with volumetric heat sources
675 throughout the core. Their model matched the dipole–quadrupole dominance and axisymmetry in
676 Mercury observations, but it did not reproduce the relatively low strength of Mercury's field.
677 The likelihood that such a thermal perturbation is present at Mercury's CMB is also unclear. In
678 contrast, a numerical dynamo model by Tian *et al*. (2015) instead imposed a north–south
679 antisymmetric thermal perturbation (i.e., of spherical harmonic degree 1) at the CMB (Figure
680 19.3), resulting in higher heat flux in the northern hemisphere. In addition, a thin, stably
681 stratified layer was imposed at the top of the core in this model. This combination of properties
682 resulted in a magnetic field that reproduced the dipole–quadrupole dominance, axisymmetry, and

683 the weakness of Mercury's field. The north–south antisymmetric thermal perturbation in this
684 model was justified on the basis of the concentration of smooth plains in Mercury's northern
685 hemisphere (Head *et al.*, 2011).

686 Recent work by Philpott *et al*. (2014) also suggested that there has been little to no secular
687 variation in the large-scale magnetic field components between the time of the Mariner 10 flybys
688 (1974–1975) and the four years that MESSSENGER was in orbit about Mercury. A study by
689 Stanley and Bloxham (2016) of the Saturnian dynamo suggests that if Mercury possesses a stably
690 stratified layer at the top of the core, and if the magnetic field is very axisymmetric, then very
691 slow secular variation of the field is a natural result. This correspondence between slow secular
692 variation and a stably stratified layer may help to explain the lack of observed secular variation
693 in Mercury's magnetic field.

694

695 ***19.4.4 Core properties***

696 The relative dominance of Mercury's core as a fraction of the planet's mass and volume
697 (Chapter 4) underscores the influence of the core in the planet's overall evolution. The basic
698 properties of the core, and particularly its thermodynamic attributes, are critical for
699 understanding how it has evolved. Siegfried and Solomon (1974) utilized a thermal conduction
700 model for heat transport through the planet, in concert with knowledge of the thermodynamic
701 properties of iron for the core, to investigate the thermal history and core crystallization of
702 Mercury. More recent approaches have generally considered heat transport through the mantle
703 via convection and various alloys of iron and sulfur for the core (e.g., Schubert *et al*., 1988;
704 Hauck *et al*., 2004; Grott *et al*., 2011; Tosi *et al*., 2013).

705 Over the past two decades, knowledge of the behavior of a variety of potential core-forming
706 materials has grown considerably. The pressures within Mercury's core, ~5–40 GPa (Hauck *et*
707 *al*., 2013), are directly accessible in laboratory experiments. Of particular interest are the
708 temperature and pressure dependencies of the properties of iron alloys, including the thermal
709 conductivity, thermal expansivity, and melting behavior. It is well-known that Fe–S alloys have
710 the peculiar behavior that their eutectic melting temperature decreases with increasing pressure
711 (e.g., Fei *et al.*, 1997; Fei *et al.*, 2000; Li *et al.*, 2001; Chudinovskikh and Boehler, 2007; Stewart
712 *et al.*, 2007; Chen *et al.*, 2008) up to 14 GPa with shifts in the eutectic composition toward more
713 Fe-rich compositions at pressures up to at least 40 GPa (Stewart *et al*., 2007).
714 Iron–silicon alloys, which may be present in the core as a consequence of Mercury's
715 chemically reduced conditions (see section 19.4.1), behave differently from alloys of iron and
716 sulfur. The primary distinctions are that the presence of silicon results in a smaller melting point
717 depression than with S and the Fe–Si alloys show a strong solid solution (Kuwayama and Hirose,
718 2004), particularly when compared with the limited solubility of S in solid Fe, even at high
719 pressure (Li *et al*., 2001). Furthermore, temperature differences between the liquidus and solidus
720 are <50 K and the compositional differences between coexisting liquid and solid are <2 wt % Si
721 on the Fe side of the eutectic in this system at 21 GPa (Kuwayama and Hirose, 2004). In
722 contrast to the Fe–S system, it appears that the eutectic temperature increases with pressure
723 (Kuwayama and Hirose, 2004; Morard *et al.*, 2011; Fischer *et al.*, 2013) up to at least 50 GPa,
724 and the Si content of the eutectic composition increases with pressure up to at least 21 GPa
725 (Kuwayama and Hirose, 2004).
726 The more likely situation is that Mercury's core contains multiple alloying elements,
727 particularly S and Si (e.g., Chapter 2; section 19.4.1) because of a broad trade-off from S- to Si-

728 bearing Fe alloys as a function of decreasing oxygen fugacity, with mixtures of the two quite
729 likely (Malavergne *et al*., 2010; Hauck *et al*., 2013; Chabot *et al*., 2014). Depending on the
730 composition of the core, liquid immiscibility at pressures less than 12 GPa is possible, with the
731 result that S- and Si-rich liquids would separate due to their differential buoyancy and would
732 lead to a S-rich liquid at the top of the core (section 19.4.2) – though recent experiments suggest
733 that a single miscible Fe–S–Si liquid is more likely (Chabot *et al*., 2014).

734 In addition to the melting behavior of Fe–rich alloys likely to be present in Mercury's core,
735 there are other thermodynamic properties of these materials critical to the planet's evolution.
736 Among the most relevant is the thermal expansivity of these alloys, which is a controlling
737 parameter in both the temperature gradient and in the amount the planet expands or contracts
738 with temperature changes (Siegfried and Solomon, 1974; Schubert *et al.*, 1988; Hauck *et al.*,
739 2004; Williams, 2009; Grott *et al.*, 2011; Hauck *et al.*, 2013; Tosi *et al.*, 2013; Jing *et al.*, 2014).
740 Measurement of the thermal expansivity of Fe alloys is challenging, particularly at high pressure
741 and for liquids. The majority of pre-MESSENGER-era models of Mercury's interior were
742 predicated on a constant value for thermal expansivity in the core (e.g., Siegfried and Solomon,
743 1974; Schubert *et al*., 1988; Hauck *et al*., 2004; Grott *et al*., 2011), consistent with expectations
744 for Earth's core. However, the thermal expansivity is clearly a function of pressure and
745 composition (e.g., Williams, 2009), and recent work on both the internal structure (Smith *et al.*,
746 2012; Hauck *et al.*, 2013; Rivoldini and Van Hoolst, 2013; Chapter 4) and the contraction of
747 Mercury (Tosi *et al*., 2013) has aimed to accommodate this variation. Recent experimental
748 measurements of the density and sound velocity of Fe alloys at high pressure and temperature
749 have altered our understanding of the variation in core thermal gradients and the potential for
750 contraction in these relevant systems, particularly for Fe–S alloys (Jing *et al.*, 2014). The

751 primary consequence of these new data and models is the potential for steeper adiabatic thermal
752 gradients and larger amounts of thermal contraction than previously appreciated.
753 The thermal conductivity of Fe alloys is particularly important for understanding both core
754 heat transfer and the evolution of Mercury's magnetic field. Recent experimental and numerical
755 estimates of the thermal conductivity of iron and Fe alloys at the conditions of Earth's core are
756 greater than previous canonical values by a factor of 2–3 (e.g., de Koker *et al.*, 2012; Pozzo *et*
757 *al.*, 2012; Gomi *et al.*, 2013), leading to questions regarding the relative role of thermal
758 buoyancy in driving Earth's dynamo. However, molecular dynamics calculations by Zhang *et al*.
759 (2015) are more consistent with lower values of the conductivity, as are recent direct
760 measurements of thermal conductivity of solid iron at high pressure (Konôpková *et al*., 2016).
761 At Mercury's core conditions, experimental work also appears to suggest a larger thermal
762 conductivity in pure Fe (Deng *et al.*, 2013b) than is typically found in models of the planet's core
763 heat transport and magnetic field generation. Moreover, Si is known to substantially decrease
764 the thermal conductivity in Fe alloys (Seagle *et al.*, 2013), perhaps reducing even the larger
765 estimates of thermal conductivity toward the values assumed for Mercury's core in previous
766 models of the planet's interior. Ultimately, the thermal conductivity of Mercury's core depends
767 on pressure, temperature, and composition and plays a major role in the thermal gradient and the
768 longevity and pervasiveness of core convection necessary for driving the magnetic field.
769
770
771 **19.5 Thermo-chemical models of interior evolution**
772 The volcanic and tectonic evolution of Mercury as recorded on its surface is closely
773 connected to the amount of heat in, and the transfer of that heat from, the planet's interior.

Therefore, understanding Mercury's geologic evolution also requires an understanding of the processes acting in the deep interior. Thermal or thermo-chemical evolution models are usually employed to shed light on the working of a planet's interior heat engine (Solomon, 1977; Stevenson *et al.*, 1983; Schubert *et al.*, 1988; Hauck *et al.*, 2004; Redmond and King, 2007; King, 2008; Grott *et al.*, 2011; Michel *et al.*, 2013; Tosi *et al.*, 2013). In order to understand the evolution of the entire planet we utilize models of planetary evolution that incorporate crucial thermal, chemical, magmatic, and tectonic processes constrained by MESSENGER observations.

### *19.5.1 Modeling approaches*

The most straightforward models of the internal evolution of planets consider the global energy balance for the mantle and core via the relations

$$\rho_{\mathrm{m}} c_{\mathrm{m}} V_{\mathrm{m}} \frac{dT_{\mathrm{m}}}{dt} = -q_{\mathrm{m}} A_{\mathrm{m}} + Q_{\mathrm{m}} V_{\mathrm{m}}$$

$$\rho_{\mathrm{c}} c_{\mathrm{c}} V_{\mathrm{c}} \frac{dT_{\mathrm{c}}}{dt} = -q_{\mathrm{c}} A_{\mathrm{c}} + Q_{\mathrm{c}} V_{\mathrm{c}}$$

where $\rho$ is density, $c$ is the heat capacity, $V$ is volume, $T$ is temperature, $A$ is surface area, and the subscripts m and c refer to the mantle and core, respectively. $Q$ is the rate of heat released in the interior per unit volume by the decay of the long-lived radioactive elements $^{40}$K, $^{232}$Th, and $^{238}$U, and $q_{\mathrm{c}}$ and $q_{\mathrm{m}}$ are the heat flow out of the core and the mantle, respectively. A model based on the above energy balance is generally sufficient to quantify the amount of secular cooling of the planet, and parameterizations for the heat flow values $q_{\mathrm{m}}$ and $q_{\mathrm{c}}$ derived from scaling relations between key dimensionless numbers are usually employed to describe the heat transport from the

795 mantle to the surface (e.g., Moresi and Solomatov, 1995; Grasset and Parmentier, 1998; Reese *et*
796 *al.*, 1998), where heat is ultimately radiated to space.

797 Perhaps the most important parameter for governing how heat moves through a planetary
798 mantle is the solid-state viscosity. The mantle viscosity has a strong dependence on temperature
799 such that the cool, outermost portion of the planet is rigid, yet at temperatures several hundred to
800 a thousand degrees hotter mantle material behaves like a slow-moving fluid. A consequence of
801 this behavior for most planets is that an immobile upper layer called a stagnant lid rapidly
802 develops. This situation is in contrast to the mechanism of plate tectonics operating on Earth.
803 The slow diffusion of heat from the interior through the thick stagnant lid is considerably less
804 efficient than the advectively dominated heat transport from lithospheric recycling in plate
805 tectonics. As a result, cooling is slow in most planets, and the interior is kept warm over
806 extended periods of time.

807 Planetary thermal evolution calculated via the parameterized energy balance approach can
808 then be combined with a model of mantle melting behavior to quantify the amount of melt
809 generated in the interior (e.g., Hauck *et al.*, 2004, Grott *et al.*, 2011). With limited melting
810 experiments tailored to the low-Fe and highly reducing conditions in Mercury's mantle, the well-
811 characterized solidus of terrestrial KLB-1 peridotite has often been used as a proxy for the
812 mantle solidus (e.g., Herzberg *et al.*, 2000). In these one-dimensional parameterized mantle
813 convection models, melt is then generated whenever the mantle temperature exceeds the model
814 solidus and is assumed to be extracted instantaneously, whereas the melt region is replenished
815 with undepleted material on a timescale associated with the mantle convection speed. A general
816 sketch of the relevant temperatures in the interior and the generation of partial melt is shown in
817 Figure 19.4.

One of the major constraints on models of the thermo-chemical evolution of Mercury is how much the planet has radially contracted as documented by its surface tectonic landforms (Chapter 10; Section 19.3.2). Three global processes contribute to radial contraction, and the magnitude of each can be estimated once the thermo-chemical evolution of mantle and core has been calculated (Hauck *et al*. 2004; Grott *et al*., 2011; Tosi *et al*. 2013). Cooling causes the mantle and core to contract, resulting in a contribution $\Delta R_{\mathrm{th}}$ to the change in planetary radius. Phase changes in the core and mantle can result in changes in the specific volume of their constituent materials, which further contribute to a change in the radius of the planet. Usually, consideration of phase changes is restricted to partial melting of the mantle and freezing of an inner core. The products (i.e., crust and the mantle residuum) of mantle differentiation have a larger volume than the primordial mantle, resulting in a net expansion, $\Delta R_{\mathrm{md}}$, of the planet (Kirk and Stevenson, 1989). However, solidification of the solid inner core results in a decrease in volume and a hence a radial contraction, $\Delta R_{\mathrm{ic}}$ (Solomon, 1976). However, with Si present in the core, the density difference between the liquid and solid phase will be small as a result of the nearly similar compositions of the two phases. In total, the radius change of the planet can be expressed as the sum of the individual contributions

$$\Delta R_{\mathrm{p}} = \Delta R_{\mathrm{th}} + \Delta R_{\mathrm{md}} + \Delta R_{\mathrm{ic}}$$

where the details of the amount of radius change depend on the assumed chemical composition of mantle and core as well as on the associated thermal expansion coefficients (e.g., Grott *et al.*, 2011; Tosi *et al.*, 2013).

Whereas one-dimensional models have been shown to be sufficient to study the global evolution in terms of secular cooling, crustal production, and planetary contraction (Tosi *et al.*, 2013), more complex two- and three-dimensional models are necessary to understand the

841 planform of mantle convection, the efficiency of mantle mixing, and the persistence of mantle
842 convection to the present (Redmond and King, 2007; King, 2008; Michel *et al.*, 2013; Tosi *et al.*,
843 2013). Instead of parameterizing the heat flow into and out of the mantle, such models involve
844 self-consistent solutions to the equations of mass, energy, and momentum transport in the mantle
845 and directly calculate convective velocities and the temperature distribution in the interior. The
846 chemical composition of the mantle is often tracked with particle tracers (Plesa *et al.*, 2013; Tosi
847 *et al.*, 2013), and the resulting buoyancy is included in the momentum conservation equation.
848 The increase in model detail of two- and three-dimensional simulations comes at the price of
849 higher computational cost, and running a large number of Monte-Carlo style simulations, as is
850 increasingly common with one-dimensional models, becomes prohibitively expensive for fully
851 dynamical models. Instead, the parameter space is usually sampled with a few representative
852 models. Depending on the aim of the investigation, model complexity can be reduced by
853 considering two-dimensional models (Redmond and King, 2007; Michel *et al*., 2013), or by
854 disregarding crustal production (Redmond and King, 2007; King, 2008) or mantle mixing of
855 melt residuum (Redmond and King, 2007; King, 2008; Michel *et al*., 2013).
856 The other major constraint on the internal evolution of Mercury is its internally generated
857 magnetic field. A magnetic field generated by a core dynamo requires fluid motions within the
858 electrically conductive fluid portion of the core. A commonly employed minimum, though not
859 necessarily sufficient, requirement for dynamo generation is that if the motions are the result of
860 thermal convection then the core heat flux must exceed the amount of heat that can be
861 transported by thermal conduction along the adiabatic thermal gradient that convection imparts.
862 Energy for driving convective motions also may be derived from compositional buoyancy, such
863 as is generated by the expulsion of a relatively light element rich fluid upon the crystallization of

the core. It has also been suggested (e.g., Christensen, 2006) that Mercury's core may not be entirely convecting and could instead have a stable layer at its top that may account for its relatively weak magnetic field (see section 19.4.3). In both of these latter cases, the heat flux at the CMB flows from the core to the mantle but may be less than can be conducted along the adiabatic thermal gradient, with convection restricted to deeper portions of the core.

### *19.5.2 Persistence of mantle convection*

Mercury's large core and relatively thin silicate shell raise important questions about how the planet has cooled through its history, in particular the role of mantle convection. These questions are important because upwelling mantle is generally a critical ingredient in magma generation, and convection leads to larger rates of cooling that help drive the fluid flow in the core necessary for magnetic field generation. Solid-state convection within a layer in a planetary body depends on several material properties as well as the temperature contrast across the layer and depends strongly on the thickness of that layer. For bottom-heated convection, the vigor of mantle convection is described by the non-dimensional mantle Rayleigh number

$$Ra = \frac{\rho g \alpha \Delta T D^3}{\kappa \eta}$$

where $\rho$ is density, $g$ is gravitational acceleration, $\alpha$ is thermal expansivity, $\Delta T$ is the temperature difference across the convecting layer, $\kappa$ is thermal diffusivity, $\eta$ is mantle viscosity, and $D = R_p - R_c$ is the thickness of the convecting layer, where $R_p$ is the planetary radius and $R_c$ is the core radius. Convection requires that $Ra$ be larger than some critical value, and above that value the vigor of convection increases with $Ra$. Therefore, mantle convection is more difficult in a thin mantle than in a thicker one because of the cubic dependence on layer thickness. As a consequence, mantle convection in Mercury is expected to be sluggish compared with convection in planets with thicker mantles. Furthermore, mantle cooling can result in a transition

887 from convection to thermal conduction in the mantle if the Rayleigh number falls below its
888 critical value. The cessation of mantle convection would result in the end of pressure-release
889 melting during convective ascent and most likely the end of global-scale volcanism, though local
890 volcanism could continue, such as observed in impact basins and sites of small-scale explosive
891 volcanism (Chapter 11).

892 As a result of Mercury's thin mantle, predictions of rather modest internal heat production,
893 and the strong temperature-dependence of the viscosity of mantle rocks, questions were raised in
894 the pre-MESSENGER era about the persistence of mantle convection to the present. Some
895 studies with one-dimensional parameterized convection models found that, although convection
896 was important for much of the planet's history, it may have ceased before the present (Hauck *et*
897 *al*., 2004). However, other work with two- and three-dimensional fluid dynamic models (Breuer
898 *et al.*, 2007; Redmond and King, 2007), as well as studies with one-dimensional models that
899 considered the insulating capacity of the near-surface regolith and crust (Grott *et al.*, 2011),
900 generally found that mantle convection persisted throughout the planet's history.

901 MESSENGER's observations of Mercury have substantially improved our understanding of
902 the planet's interior and so have helped refine many of the assumptions and boundary conditions
903 required for models of its internal evolution. The most important of these constraints are the
904 improved knowledge of radiogenic heat production (Peplowski *et al.*, 2011, 2012) and the
905 thickness of the outer solid shell of the planet (Chapter 4). Typically, earlier work was based on
906 the assumption that the core–mantle boundary was ~600 km deep compared with the ~420 km
907 determined by MESSENGER (Hauck *et al.*, 2013).

908 That data from MESSENGER indicate Mercury's silicate shell is nearly one-third thinner
909 than in previous models has led to a reevaluation of whether mantle convection continued

910 throughout the planet's history. Furthermore, although the precise partitioning of heat-producing
911 elements between the near surface (where they have been measured) and the interior is only
912 weakly constrained, the relative amounts of U, Th, and K, as well as their surface abundances,
913 provide important (and previously unavailable) constraints. Indeed, the finding of surprisingly
914 abundant K (Peplowski *et al.*, 2011, 2012) is important for quantifying Mercury's internal
915 evolution because of the strong heat output of $^{40}$K coupled with its relatively shorter half-life
916 than the long-lived isotopes of U and Th. Taking these new data into account, Michel *et al*.
917 (2013) reevaluated the issue of convection within Mercury's mantle utilizing two-dimensional
918 axisymmetric, spherical shell fluid dynamic calculations. They found that, for a broad range of
919 conditions of mantle heat production, mantle viscosity, and initial internal temperatures,
920 cessation of mantle convection within the past several billion years is common in models with
921 silicate layers less than ~440 km thick. These results are consistent with those of Tosi *et al*.
922 (2013), who evaluated the internal evolution of Mercury in one-, two-, and three-dimensional
923 models of mantle convection additionally constrained by ~3 km of global radial contraction as
924 had been inferred from mapping ~21% of Mercury's surface by Di Achille *et al*. (2012). In the
925 models of Tosi *et al.* (2013), cessation of mantle convection within the past 1–1.5 Gyr was the
926 norm. However, the 5–7 km of radial contraction inferred from more recent global mapping
927 (Byrne *et al.*, 2014) warrants additional thermal evolution calculations, because a larger total
928 cumulative contraction may require higher rates of cooling that may be more consistent with
929 prolonged mantle convection than with thermal conduction only. As a result of its small
930 obliquity, its proximity to the Sun, and its 3:2 spin–orbit resonance (Chapter 4), Mercury has
931 large spatial variations in surface temperature. By including the latitudinal variation in
932 temperature, Michel *et al*. (2013) found that cessation of mantle convection may be delayed by a

few hundred million years relative to typical models with a spatially constant surface temperature.

With a Monte-Carlo approach and the inferred magmatic evolution and global contraction as model constraints, Tosi *et al*. (2013) determined the times at which convection stopped in one-dimensional models of Mercury's thermo-chemical evolution. An update of their calculations, taking into account the larger amount of global contraction and the observation that Mercury had an ancient magnetic field as well as a modern one, is shown in Figure 19.5. In all, about 40% of the models consistent with the presently available constraints are found to convect to the present. This outcome is a direct consequence of the more recent estimate of global contraction, which allows for Mercury to have experienced more efficient mantle cooling than in the models of Tosi *et al*. (2013), which permitted only 3 km of contraction and had vanishingly few outcomes in which mantle convection operated at present.

### *19.5.3 Internal evolution models consistent with observational constraints*

Our current understanding of the timing of major processes in Mercury's evolution, as described in the preceding sections, is summarized in Figure 19.6. Evidence from the first ~500 Myr is limited mainly as a result of resurfacing by intercrater plains formation and impact cratering before and during the late heavy bombardment. An internally generated magnetic field was active prior to 3.7–3.9 Ga (Johnson *et al.*, 2015; Chapter 5) and is active today (Ness *et al.*, 1976; Ness, 1979; Anderson *et al.*, 2011, 2012), implying a cooling core within which either thermal or chemical convection operated during each era. The magnetic field history between ~3.8 Ga and the present is presently unknown, and either a continuously operating core dynamo or an early shutdown of the dynamo followed by a later reinitialization are plausible scenarios

(Chapter 5). Effusive volcanism was widespread early in Mercury's recorded history (e.g., Marchi *et al.*, 2013), and the areal extent of volcanism waned rapidly from the LHB until perhaps ~3.5 Ga, after which effusive activity largely ended, with the exception of local activity within younger impact basins (Prockter *et al.*, 2010; Denevi *et al.*, 2013a; Byrne *et al.*, 2016; Chapter 11). Explosive volcanism continued for a longer time period than did widespread plains volcanism (Kerber *et al.*, 2009; Thomas *et al.*, 2014). The global contraction accumulated on shortening tectonic landforms records planetary cooling from the end of the LHB to the present (Chapter 10).

Following the approach of Tosi *et al*. (2013), the range of models that satisfy the following major constraints can be determined. Successful models must (1) produce at least 5 km of crust by partial melting of the mantle, which is a minimal requirement for producing the intercrater and smooth plains, (2) show 5 to 7 km of global contraction following the end of the late heavy bombardment, and (3) exhibit heat flow from the core that would permit, though not require, the generation of a magnetic field. It is worth noting that the choice of the thickness of extracted crust has little influence on the results, as long as some crust is produced. Furthermore, the requirement on heat flow from the core serves to reject those models that would preclude a thermally driven core dynamo during the earliest evolution, but is not particularly restrictive later in the planet's history as core heat flux is generally small after 4 Gyr of evolution.

Models that satisfy all of these constraints show some common trends. Slow cooling of the planet is required, and model mantle reference viscosities at 1600 K range from $10^{20}$ to $10^{22}$ Pa s. Additionally, most models also show an early phase of mantle heating, whereas the core cools monotonically throughout evolution. Also, although up to 100 km of crust can be produced, most models produce less than 75 km. Furthermore, surface heat flow declines from about 30 mW/m$^2$

979 at the beginning of evolution to ~10 mW/m$^2$ today, consistent with an estimate derived from
980 tectonic modeling (Egea-González *et al.*, 2012). Finally, and most interestingly, the ratio of the
981 concentration of heat-producing elements in the crust to that in the primordial mantle is found to
982 be between 2 and 4.5, which is similar to the results obtained by Tosi *et al*. (2013) for a core
983 radius of 1940 km. On the other hand, the initial mantle temperature in the models is poorly
984 constrained and can range from 1600 to 1900 K, similar to the range in initial core temperature.
985 A typical thermo-chemical evolution model that satisfies the above constraints is shown in
986 Figure 19.7, where the core and mantle temperature; the core, mantle, and surface heat flow; the
987 radius change from thermal contraction and mantle differentiation; and the crustal thickness,
988 stagnant lid thickness, and extent of the partial melt zone are shown as functions of time. In this
989 model, the initial mantle temperature is 1700 K, the initial core temperature is 1875 K, the
990 crustal thermal conductivity is 2.5 W m$^{-1}$ K$^{-1}$, a poorly conducting regolith layer 5 km thick and
991 with a thermal conductivity of 0.2 W m$^{-1}$ K$^{-1}$ is included, and the mantle viscosity is $10^{20.5}$ Pa s.
992 With surface abundances of radiogenic elements of 1288 ppm $^{40}$K, 155 ppb $^{232}$Th, and 90 ppb
993 $^{238}$U (Peplowski *et al.*, 2012) and a crustal enrichment factor of 3.5, this typical model has bulk
994 silicate concentrations of heat-producing elements of 368 ppm $^{40}$K, 44 ppb $^{232}$Th, and 25 ppb
995 $^{238}$U, similar to values for Earth and Mars. Following the late heavy bombardment (i.e., ~3.8
996 Ga), the model monotonically cools at a rate of 40 K Gyr$^{-1}$, with the core and mantle cooling at
997 the same rate. Global crustal production ceases around 2.5 Ga (though is largely complete nearly
998 1 Gyr earlier), and a total of 25 km of crust is produced, resulting in a final crustal thickness of
999 30 km. Total radial contraction is just short of 7 km, with continuous accumulation of
1000 contraction following the late heavy bombardment. It is worth noting that care must be taken
1001 when interpreting the timing of crustal production from such one-dimensional models, as this

1002 timing can differ considerably from that determined with fully dynamical two- or three-
1003 dimensional models, which generally have crustal production concentrated earlier in the planet's
1004 evolution but result in similar total crustal thickness values (e.g., Tosi *et al*., 2013).

1005 Given the uncertainties associated with the state and composition of Mercury's core, the
1006 model shown in Figure 19.7 focuses on the most robust aspects of the core and considers only
1007 thermal contraction of the core and does not take into account contraction by core solidification.
1008 Although, for a given amount of inner core growth, this solidification could be a major
1009 contribution to planetary contraction for an Fe–FeS core composition (e.g., Solomon, 1976;
1010 Schubert *et al.*, 1988; Knibbe and van Westrenen, 2015), it would be less so if Si were the major
1011 alloying light element in the core (Fei *et al.*, 2011) as the density difference between solid and
1012 liquid would be smaller because of the very small difference in Si content between solid and
1013 liquid (Kuwayama and Hirose, 2004). However, the melting behavior of core material is an
1014 important factor in core contraction arising from crystallization: S-bearing cores would
1015 experience less inner core growth due to the stronger melting point depression relative to Si-
1016 bearing alloys. The true contribution of core freezing to global contraction will likely fall
1017 between these two limiting cases, but this effect is difficult to quantify without further data on
1018 the equation of state of the Fe–S–Si system. More importantly, it is clear that there is little room
1019 for a large contribution to the observed global contraction from core crystallization. The
1020 solidification of a large volume fraction of the core would lead to significantly more total
1021 contraction than that from thermal contraction alone, e.g., crystallization of > 2.5% the volume
1022 of the core (equivalent to an inner core <30% of the radius of the core) would lead to at least 2
1023 km of additional contraction (Grott et al., 2011). Thus, the contribution of core crystallization is
1024 likely limited, as fewer models would be permitted because they would exceed the 7 km of radial

contraction accommodated by tectonic deformation and even the 9 km inferred for total planetary contraction that includes the elastic accommodation of radial contraction prior to the formation of major faults (Chapter 10). This result implies that either core solidification was close to complete by the end of the late heavy bombardment, or that only a small inner core started freezing in the recent past. Because of indications that the inner core is likely small (Chapter 4), the latter scenario is more likely.

A three-dimensional view of the thermal evolution of a model with the same properties as discussed above is shown in Figure 19.8. Additionally, the surface temperature variation imposed by Mercury's 3:2 spin–orbit resonance is taken into account (Chapter 4). The model is similar to that presented by Tosi *et al*. (2015), in which chemical composition is tracked with a particle tracer technique (Plesa *et al.*, 2013), and uses the same initial conditions as the model shown in Figure 19.7. Figure 19.8a shows the variation of average annual surface temperature, which ranges from 260 to 430 K between the poles and the equatorial regions. The mantle convection pattern shown in Figure 19.8b reflects this type of temperature distribution, with downwellings (blue) more focused near the polar regions. As a result of the small thickness of Mercury's mantle, the convective pattern shows only small-scale up- and downwellings, and the more linear structures found in earlier simulations of mantle convection with a mantle thickness of 600 km (King, 2008) are not reproduced. Toward the end of the model run, mantle convection ceases, resulting in a conductive temperature profile in the mantle (Figure 19.8c). In this model, modern mantle temperatures reflect the forcing imposed by the insolation pattern. However, it should be noted that it takes a few hundred million years for the perturbation from insolation to diffuse to any meaningful depth. Therefore, the full extent of the temperature forcing will be

1047 reflected in the deep interior only if the 3:2 spin–orbit resonance has been stable for an extended
1048 period of time (Correia and Laskar, 2004; Noyelles *et al.*, 2014).

1049 Although the general picture of Mercury's thermo-chemical evolution is consistent with the
1050 constraints provided by MESSENGER observations, details of the models may change as more
1051 data are analyzed and eventually provided by new missions such as BepiColombo (Chapter 20).
1052 In particular, the amount of radial contraction documented in shortening tectonic structures has
1053 been continuously refined (Strom *et al.*, 1975; Watters *et al.*, 2009; Di Achille *et al.*, 2012; Byrne
1054 *et al.*, 2014), resulting in less stringent constraints on Mercury's thermal evolution. Current best
1055 estimates for the total radial contraction accumulated by brittle structures since the late heavy
1056 bombardment range from 5 to 7 km (Byrne *et al.*, 2014) but may be as large as ~9 km when
1057 elastic deformation is considered, or less than 5 km if the dip angles of the thrust faults are
1058 uniformly and surprisingly steep (Chapter 10). Importantly, larger values (> 7 km) of contraction
1059 would allow for lower mantle viscosities and thus more efficient mantle convection.
1060 Alternatively, such greater contraction could also allow for a larger contribution of core
1061 solidification to the total contraction of Mercury, depending on core composition, or more likely
1062 some combination of increased cooling and core solidification.

1063 ***19.5.4 Other factors influencing Mercury's thermo-chemical evolution***

1064 One of the factors not considered in the above models is the potential presence of heat-
1065 producing elements in Mercury's core. At the low oxygen fugacities inferred from the high S
1066 abundance and low FeO content in Mercury's crust (Zolotov *et al.*, 2013), lithophile elements
1067 such as K, Th, and U can become more siderophile (Malavergne et al., 2010). McCubbin *et al.*
1068 (2012) estimated that up to 10% of the total inventory of U and potentially Th could have
1069 partitioned into the core, thus providing an additional heat source that could slow global

1070 contraction. However, the differences in global contraction between models with and without
1071 heat-producing elements in the core have been found to be minor (Tosi *et al*., 2013), as the total
1072 inventory of heat-producing elements in the interior is only weakly affected. Partitioning of U
1073 and Th into the core tends to increase the heat flux out of the core and can extend the period
1074 during which a thermal-buoyancy-generated dynamo can operate by as much as 100 Myr.

1075 In addition to the production of partial melt in the interior, Mercury's surface compressive
1076 stress state has likely been an important factor controlling effusive volcanism. On a contracting
1077 planet such as Mercury, extrusive volcanism may be substantially inhibited as magma pathways
1078 to the surface are shut-off by maximum compressive stresses in the horizontal direction (Chapter
1079 11). Therefore, the longevity of volcanism as observed on the surface may not be a direct
1080 indicator of the timing of melt production in the deep interior. On the other hand, local factors
1081 such as variations in the thickness of an insulating crust and/or regolith layer, which would have
1082 a lower thermal conductivity than the mantle (Section 19.5.3), largely due to higher porosities
1083 (Schumacher and Breuer, 2006), are usually not fully taken into account in thermo-chemical
1084 evolution models. Therefore, local volcanism may be ongoing even if global models,
1085 particularly one-dimensional models, do not predict the production of partial melt at a given
1086 time.

1087 Another energy source not treated in the above discussion is impact heating, which would be
1088 expected to contribute to the global energy balance mainly during the early phases of Mercury's
1089 evolution. Impact heating associated with the formation of the Caloris impact basin has been
1090 modeled by Roberts and Barnouin (2012), who showed that impact heat can alter mantle
1091 dynamics. In addition to the production of melt at the impact site itself, partial melting may be
1092 induced even far from the impact. Thus, the smooth plains within and adjacent to the Caloris

basin could be at least in part the consequence of the impact itself, the heat for which is stored in the mantle over an extended period of time. On the other hand, the influence of isolated impacts on the global evolution of the planet is relatively small (Roberts and Barnouin, 2012), and the conclusions drawn from the simpler models discussed above remain essentially unchanged.

### *19.5.5 Core evolution*

MESSENGER's unveiling of Mercury's internal structure and the geometry and history of its internal magnetic field underscore the important role of the metallic core on the planet's evolution. Taken in concert with the growing understanding of the properties of materials at the conditions of Mercury's core (section 19.4.4), which indicate the potential importance of zones of top-down crystallization and liquid–liquid immiscibility, it is clear that core evolution in Mercury differed from that of Earth's core. Ultimately, models of core evolution on Mercury must account for the planet's magnetic field structure and history (Chapter 5), match the internal structure (Chapter 4), and be consistent with the magnitude of the planet's contraction (Chapter 10).

The driving mechanisms of core evolution are cooling and the chemical differentiation that results from crystallization as the core cools below its melting temperature. The rate of core cooling depends strongly on how the mantle is cooling, as all of the heat from the core must pass through the mantle on its way to the planet's surface. Early in the planet's history, core cooling may have been relatively rapid (Figure 19.7), especially if the planet was hot, because high internal temperatures reduce the viscosity of the mantle and make it easier to remove heat quickly by convection. Of course, just as the cooling of the mantle slows as its initial store of heat of formation is lost and heat production follows the decay of radioactive elements, the cooling of the core slows as well. The rate of cooling of the core is important because a source

1116 of convection is necessary to drive the motions in the electrically conductive liquid metal that
1117 generate the magnetic field. A minimum condition for thermal convection throughout the entire
1118 core is that the heat flux through the CMB must exceed that which can be conducted along the
1119 adiabat. Given a thermal conductivity of 40 W $m^{-1}$ $K^{-1}$, previous workers (Hauck *et al.*, 2004;
1120 Tosi *et al.*, 2013) found the minimum core heat flux for thermal convection to be in the range of
1121 12–19 mW $m^{-2}$ for a range of possible thermal expansivity values. Such core heat fluxes are
1122 exceeded only early in Mercury's history. The more recent, higher estimates of the thermal
1123 conductivity of pure iron at pressures near that of Mercury's CMB (Deng *et al.*, 2013b) of 40–
1124 120 W $m^{-1}$ $K^{-1}$ could increase this minimum heat flux by up to a factor of 3. Such high thermal
1125 conductivities would limit thermally driven core convection to a very short time period following
1126 planet formation. However, the presence of light alloying elements tends to decrease the thermal
1127 conductivity; for example, as little as 9 wt% Si reduces the thermal conductivity of the Fe alloy
1128 to 41–60 W $m^{-1}$ $K^{-1}$ (Seagle *et al.*, 2013) at Earth's core conditions. As Mercury's core likely
1129 hosts considerable abundances of light elements (section 19.4.1), the earlier value adopted for
1130 thermal conductivity may not be far off, though the uncertainty may be considerable.

1131 Although it is possible that Mercury's early magnetic field (Chapter 5) was driven by thermal
1132 convection, the present-day field is likely dominated by flows driven by compositional
1133 buoyancy. The simplest mechanism for generating compositional buoyancy is crystallization of
1134 a core alloy in a situation where the compositional difference between the precipitating solid and
1135 residual liquid is large, such as has been previously described in the Fe–S system. Sulfur-
1136 bearing systems are the best-studied analog for Mercury because of the broad literature on Fe–S
1137 melting and because sulfur has such a large melting point depression even at high pressure (e.g.,
1138 Fei *et al.*, 1997). The consequence of the decreasing melting and eutectic sulfur contents with

1139 increasing pressure (section 19.4.4) is that, if the core is comprised of an Fe–S alloy, then it is
1140 likely that the crystallization of core material at these pressures began at the top, rather than the
1141 bottom, of the core (Hauck *et al.*, 2006; Stewart *et al.*, 2007; Chen *et al.*, 2008; Williams, 2009).
1142 An interesting consequence of the combination of the shifts in eutectic temperature and
1143 compositions, which vary with pressure, is that two radially separated regions of the core may
1144 experience such top-down crystallization, also termed Fe snow (Chen *et al*., 2008).

1145 Both pre- and post-MESSENGER models (Chen *et al.*, 2008; Dumberry and Rivoldini, 2015)
1146 of an Fe–S core indicate multiple modes of crystallization, including bottom-up (like Earth) and
1147 top-down (Fe snow). In such a system, at low sulfur contents of ~5 wt % or less and with small
1148 inner cores, Dumberry and Rivoldini (2015) found that bottom-up crystallization would be
1149 expected. However, those workers did not model the non-ideal mixing behavior observed at 14
1150 GPa in the Fe–S system (Chen *et al.*, 2008), which essentially requires a zone of Fe snow
1151 between 10 and 14 GPa at even very small sulfur contents because the decrease in melting
1152 temperature is so large. With larger sulfur contents or with larger inner core sizes, various top-
1153 down crystallization regimes are possible, whether there is a layer of crystallizing material
1154 overlying a layer in which the Fe snow re-melts, whether the crystallizing material simply falls to
1155 the top of the growing inner core (Hauck *et al.*, 2006; Dumberry and Rivoldini, 2015), or even if
1156 there is a second layer of top-down crystallization (Chen *et al.*, 2008).

1157 Top-down crystallization is a consequence of a situation in which the melting temperature
1158 increases as a function of depth more slowly than the actual temperature (Hauck *et al.*, 2006;
1159 Williams, 2009). In the Fe–S system there is a marked decrease in the eutectic melting
1160 temperature with increasing pressure, as well as a reduction in the S content of the eutectic with
1161 increasing pressure, both of which lead to melting temperatures decreasing with depth for a wide

range of bulk compositions. Measurements of the density and sound velocity of Fe–S liquids at high pressure also indicate that S tends to result in larger adiabatic temperature gradients relative to pure Fe liquids, enhancing this effect and extending to even lower sulfur contents (Jing *et al.*, 2014). As a result of the small melting point reduction in Fe–S alloy cores with low abundances of S, such systems tend to have large inner cores, which in turn tends to concentrate S in the outer core because of the low solubility of S in solid Fe. As a consequence, Fe–S-dominated cores are likely to have experienced Fe-snow regardless of their composition. However, such large inner cores are not favored in structural models constrained by Mercury's rotational dynamics (Chapter 4).

Even though our understanding of the evolutionary paths of Mercury's core under scenarios in which sulfur is the sole light element is becoming more mature, it is also clear that other light elements in addition to, or instead of, sulfur are likely present in the core (Section 19.4.1; Chapter 2). As noted above, carbon is generally a siderophile element, but it has been suggested that C is present as graphite in the mantle and that graphite may have formed an early floatation crust on the planet (Vander Kaaden and McCubbin, 2015), an idea that is consistent with spectral reflectance and neutron spectroscopy observations of the surface (Murchie *et al.*, 2015; Peplowski *et al.*, 2015a, 2016). Consequently, if the core and mantle formed in equilibrium then the core may be saturated in C, although the total amount would be small as the maximum solubility of C in Fe is ~4 wt % and that value decreases with increasing pressure (Lord *et al.*, 2009). This value would be larger if $Fe_3C$ were present, but the density and compressibility of C-bearing alloys are such that it would be difficult for C to be the sole light element in Mercury's core. However, the consequences of even some C being present might be important. For

example, the decreasing amount of C in eutectic melts with increasing pressure in the Fe–$Fe_3C$ system is consistent with top-down crystallization, even without S.

In contrast, the presence of silicon, which is likely because of the planet's strongly reducing conditions (see sections 19.4.1 and 19.4.4), has rather different implications for the evolution of the core. The melting behavior of Si-bearing Fe alloys at conditions appropriate to Mercury is more poorly known than for alloys with S or even C. The phase diagram of Fe–FeSi at 21 GPa determined experimentally by Kuwayama and Hirose (2004) is instructive, as they found that the eutectic point is at both a higher temperature and a larger Si abundance than at 100 kPa (1 bar). They also found, as noted above, that the difference in composition between the coexisting solid and liquid phases at temperatures between the solidus and liquidus on the Fe side of the eutectic is very small: a maximum of ~2 wt % Si between the solid and liquid phases. An important consequence of this behavior is an Earth-like bottom-up crystallization of the core, but with residual liquids left by crystallizing of Fe–Si core material that would be only marginally less dense than surrounding material, limiting the buoyancy available to drive convection were the core sufficiently chemically reduced that silicon were the only light alloying element present.

Perhaps most critical to understanding the evolution of Mercury's core is the behavior of Fe alloys with combinations of S, Si, and possibly C. Despite the fact that the thermodynamic properties of multi-component Fe alloys are less well known than for the binary systems, the data that are available suggest interesting evolutionary paths for Mercury's core. For example, liquid immiscibility, such as displayed in both Fe–S–C (e.g., Dasgupta *et al.*, 2009) and Fe–S–Si liquids (section 19.4.1), has potential consequences for compositional segregation within the outer core. Fe–S–C immiscibility would have an influence within only a relatively thin layer near Mercury's CMB because immiscible behavior occurs only at pressures less than 6 GPa

(Dasgupta *et al.*, 2009), which is close to the possible CMB pressure (Chapter 4). However, immiscibility in the Fe–S–Si system would extend deeper within Mercury's outer core (section 19.4.4). Such segregation, if present, likely developed early in the planet's history during metal–silicate differentiation and immediately thereafter. For bulk core compositions near the miscibility limit, however, there is a possibility that the progressive crystallization of a Fe–Si-rich solid and resultant increase in concentration of S in the liquid would drive Mercury's core into a liquid immiscibility state later in its evolution. For this situation to occur, however, relatively large inner core growth would be required to substantially change the outer core composition, an outcome that is inconsistent with models of Mercury's thermal contraction discussed above and estimates of the planet's internal structure (Chapter 4).

A relative lack of experimental data limits firm conclusions about the crystallization behavior in an Fe–S–Si core. Recent experimental results on the Fe–S–Si–C system (Martin *et al.*, 2015) indicate eutectic melting temperatures similar to those of the Fe–S–C system from ~4–15 GPa, with minimal pressure-dependence of the eutectic. Top-down crystallization would be favored in that system. However, data on the pressure-dependence of melting in the Fe–S–Si system are not available at present. While the melting behavior of the Fe–S and Fe–S–Si–C systems suggest that top-down crystallization is likely, the Fe–Si system appears more consistent with a bottom-up crystallization sequence; whether the effects of alloying with S or Si would dominate that behavior is unclear without further data. Determination of melting behavior in the Fe–S–Si system, and the thermodynamic properties that control the adiabatic temperature gradient, are crucially needed in order to understand more fully the crystallization of Mercury's core.

## 19.6 Discussion

MESSENGER observations have substantially altered our understanding of how Mercury has evolved over its history, but several crucial questions remain open. In particular, we are at a relatively early stage in understanding the connection between the dynamics of the mantle and the production of the crust and the generation of the magnetic field. We next discuss these issues in more detail, focusing on open questions that may be addressed through a combination of analysis of MESSENGER data, modeling, and the acquisition of new observations from BepiColombo and other future missions.

### *19.6.1 Crustal production and mantle dynamics*

Global crustal production through time is a primary indicator of the evolution of a planet – that of its crust and of the interior from which the crust was derived. For planets without crustal recycling, the crust represents a nearly complete time history of intrusive and extrusive volcanism. This history, even when known only to first order, places powerful constraints on our understanding of the evolution of the interior (e.g., Hauck and Phillips, 2002). On Mercury, the clearest constraints on crustal formation are that the best estimate of its average thickness is approximately 35 km (James *et al.*, 2015; Padovan *et al.*, 2015; Chapter 3) and that the tail end of the era of effusive volcanism postdates the Caloris impact by perhaps a few hundred million years at most (Byrne *et al.*, 2016; Chapters 6, 11). Intercrater plains, also interpreted to be dominantly volcanic in origin, are more areally extensive than the smooth plains and are in places as old as 4.0–4.1 Ga (Chapter 6). The first ~500 Myr of Mercury's surface history is also veiled by the overprinting of the late heavy bombardment. Regardless, MESSENGER observations have revealed that Mercury has experienced the most efficient and complete differentiation of mantle and crust among the terrestrial planets, and that this crust was largely

1253 built up by successive episodes of effusive volcanism that were likely largely complete within
1254 the first 1 Gyr of planet history. Given that Mercury has such a thin mantle, prone to relatively
1255 sluggish mantle flow and even the cessation of mantle convection entirely, it is remarkable that
1256 generation of the crust could have been so efficient and rapid – particularly in light of the idea
1257 that crustal products of a magma ocean may have been only meters thick (e.g., Vander Kaaden
1258 and McCubbin, 2015), leaving virtually all of the crust to be produced by serial magmatism.
1259 However, because of the low FeO content and modest pressures in Mercury's mantle, the partial
1260 melts produced throughout the mantle would be exceptionally buoyant and less susceptible to
1261 stalling during ascent (Vander Kaaden and McCubbin, 2015), perhaps facilitating such efficient
1262 crustal formation.

1263 The heterogeneity of Mercury's crustal production as observed in its geochemical diversity
1264 (e.g., Weider *et al.*, 2015; Chapters 2, 7), and the spatial distribution of smooth plains volcanism,
1265 also provide important clues to the history and dynamics of the interior. Indeed, observations by
1266 MESSENGER's suite of geochemical sensors indicate both a range of crustal compositions that
1267 point to partial melting from multiple sources (Charlier *et al.*, 2013), and a spatial heterogeneity
1268 in compositions that does not always follow geomorphological unit boundaries (Peplowski *et al.*,
1269 2015b; Weider *et al.*, 2015). Interestingly, in a manner similar to the Moon's spatial dichotomy
1270 in mare volcanism between its near and far sides, and the asymmetric concentration of volcanism
1271 on Mars near the Tharsis province, there is a distinctive spatial difference in the abundance of
1272 smooth plains units between Mercury's northern and southern hemispheres (Chapters 6, 11).
1273 The largest expanses of smooth plains reside at high northern latitudes and within and around the
1274 Caloris basin, which is also located in the northern hemisphere. Smaller areas of smooth plains
1275 are found generally in proximity to impact basins with little difference in areal coverage between

1276 the hemispheres (Chapter 6). Consequently, the processes responsible for the formation of
1277 smooth plains in the Caloris region and the northern volcanic plains may be different from those
1278 that yielded the isolated, small smooth plains units distributed more evenly throughout the
1279 northern and southern hemispheres. Any hemispherical differences in the earlier volcanic
1280 activity that produced the intercrater plains are not clear at this time, though some regions also
1281 appear to be associated with impact basins (Denevi *et al.*, 2013b). Although MESSENGER
1282 provided global geochemical coverage of Mercury, the spacecraft's highly eccentric orbit and
1283 high northern periapsis resulted in measurements only at low spatial resolution in the southern
1284 hemisphere. That these measurements cannot resolve distinct geochemical terranes in the
1285 southern hemisphere limits our understanding of the global evolution of Mercury. The planned
1286 orbit for the Mercury Planetary Orbiter on the BepiColombo mission (Chapter 20) will yield
1287 higher-resolution southern hemisphere data and may resolve additional geochemical terranes
1288 analogous to those observed by MESSENGER in the northern hemisphere.

1289 These heterogeneities in the geochemical and volcanic character of the surface are largely
1290 connected to the thermal and chemical properties of the mantle. Mercury's thin mantle yielded a
1291 style of mantle convection that was both relatively sluggish and strongly spatially restricted,
1292 because the size of individual convective cells would have been on the order of the thickness of
1293 the mantle itself. Thus, the large expanses of volcanism in the northern hemisphere require
1294 conditions that either permit extraordinarily voluminous magma production from spatially
1295 restricted upwellings or conditions that substantially altered the mantle flow dynamics from that
1296 expected on the basis of Mercury's mantle thickness. One such mechanism for altering those
1297 dynamics is a large impact, such as that which formed the Caloris basin. Indeed, the large
1298 thermal perturbation imparted by shock heating from the Caloris impact event may have led to

substantial heating of the shallow mantle beneath the impact, but it might also have enhanced some nearby, pre-existing mantle upwellings that generated magma distal from the impact site (Roberts and Barnouin, 2012). Such a mechanism could have been a major contributor to the generation of the Caloris-centric volcanism, but the northern volcanic plains do not appear to host such a large impact capable of triggering such volcanism, even though Caloris and the northern volcanic plains have indistinguishable crater size–frequency distributions and thus ages (e.g., Ostrach *et al.*, 2015). On the other hand, both the broad geochemical heterogeneity across the surface and the smaller, more distributed areas of smooth plains on Mercury could be direct consequences of the small, spatially restricted upwellings and inefficient mixing in a mantle of small thickness. This fluid dynamic behavior of the mantle could act to preserve large-scale geochemical heterogeneities, yet also focus volcanism in locally restricted areas. An important question regarding the era of dwindling effusive volcanism is the relative importance of the pattern of convection (e.g., small yet relatively abundant upwellings) to the total cooling of Mercury that led to a strongly compressive stress state, one that tended to favor intrusive over extrusive volcanic activity.

### *19.6.2 Evolution of the core and magnetic field*

The operation of an internally generated planetary magnetic field is a fundamental indicator of the dynamical behavior of the deep interior of a planet. MESSENGER observations of Mercury's magnetic field have provided important constraints on the character of field generation at present as well as early in the planet's history. Orbital measurements of the geochemical character of the surface materials, as well as gravity and rotational state determinations by MESSENGER, also help characterize the core. However, these new observations raise a number of interesting questions about the behavior of the interior over the history of the planet. In particular, the

1322 mechanism of magnetic field generation may require a number of special conditions in order to
1323 produce a weak, axisymmetric field with a large dipole offset. Further, the magnetic field, with
1324 remanent crustal magnetism indicating an ancient field in addition to the modern field, places
1325 limits on the rate of cooling over the planet's history.

1326 Although explaining Mercury's weak magnetic field has long been a challenge (e.g., Heimpel
1327 *et al.*, 2005; Stanley *et al.*, 2005; Christensen, 2006), it is the combination of the weakness of the
1328 field and its axial alignment and asymmetry about the equator that makes understanding the
1329 dynamo mechanism even more intriguing. A common thread in many models of Mercury's
1330 magnetic field is the presence of a layer stable against convection (e.g., Christensen, 2006; Vilim
1331 *et al.*, 2010; Tian *et al.*, 2015). If such a layer is present, most likely at the top of the fluid core,
1332 then the heat flux out of the core may be less than what can be conducted along the adiabatic
1333 temperature gradient. In addition, compositional stratification may also be present. As
1334 discussed above, it is quite likely that there is a thermal component to the stability of such a
1335 layer, as thermal history calculations generally predict a subadiabatic heat flux at present.
1336 Furthermore, many potential core alloy compositions favor top-down crystallization regimes that
1337 lead to compositionally stratified layers. Thus, it seems likely that Mercury's core contains a
1338 stable layer that plays a role in the strength and geometry of the planet's magnetic field.

1339 Yet the presence of a stable layer alone appears insufficient for explaining the strength and
1340 geometry of Mercury's magnetic field. To that end, recent models have included additional
1341 heterogeneity capable of further influencing magnetic field character (e.g., Figure 19.3). In
1342 particular, both Cao *et al*. (2014) and Tian *et al*. (2015) imposed laterally variable heat flux
1343 conditions at the CMB. Cao *et al.* (2014) utilized a heat flux pattern symmetric about the
1344 equator similar to the latitudinal variation in surface temperature consistent with Mercury's small

1345 axial tilt. Should the mantle be in a conductive, rather than convective state, then surface
1346 temperature variations at the surface may also have a signature at the CMB if enough time has
1347 passed since the end of the convective motions. Cao *et al*. (2014) investigated models with the
1348 highest and lowest heat flow at the equator, and they found that models with higher heat flow
1349 near the equator were better able to stabilize fields with geometries similar to those observed by
1350 MESSENGER. However, the mechanism for inducing larger heat fluxes along the equator,
1351 rather than at the poles, is unclear. Diffusion of surface temperatures to the CMB would result in
1352 relatively lower mantle temperatures near the poles, and therefore larger temperature differences
1353 and heat fluxes across the CMB there, rather than at the equator. As demonstrated in Figure
1354 19.8, the limited thickness of the mantle seems to preclude long-wavelength convective patterns,
1355 so a degree-2 style of mantle convection appears unlikely as well. Therefore, some other
1356 mechanism for inducing a symmetric equator-to-pole variation in heat flux appears necessary for
1357 this mode of dynamo generation to operate.

1358 Alternatively, Tian *et al*. (2015) imposed an asymmetric heat flux boundary condition along
1359 the CMB, with a higher heat flux out of the core near the north pole of Mercury (Figure 19.3).
1360 Those authors postulated that the higher heat flux there is a remnant of the magmatism that
1361 produced the NSP. As discussed in the previous section, there is a notable spatial dichotomy in
1362 the distribution of the youngest smooth plains on Mercury, with the largest expanses in the
1363 northern hemisphere (e.g., Ostrach *et al.*, 2015; Chapters 6, 11). However, as those volcanic
1364 deposits were emplaced 3.7–3.8 Ga, the thermal conditions that generated them are likely no
1365 longer present. Furthermore, smaller though still extensive ( $>10^5$ km$^2$ area) (Byrne *et al*., 2016)
1366 smooth plains units, the youngest effusive volcanic deposits on Mercury, are relatively well
1367 distributed between the northern and southern hemispheres, exclusive of the NSP and the plains

1368 associated with Caloris. Thus, it is worth considering whether the mechanisms for the large
1369 volcanic deposits and the smaller, more evenly distributed smooth plains deposits are the same
1370 (including whether some of the smaller deposits are even volcanic). Whereas the relatively
1371 larger concentrations of K at high northern latitudes on Mercury (Peplowski *et al.*, 2012; Chapter
1372 7) might argue for a mantle source more enriched in heat-producing elements, such enhanced
1373 heat production would in fact lead to smaller temperature contrasts and a lower heat flux across
1374 the CMB. Interestingly, the K enhancement at high northern latitudes does not respect the
1375 morphological boundaries of the northern plains, nor are the lavas in Caloris so enriched.
1376 However, if the generation of the NSP substantially depleted the mantle at high northern
1377 latitudes of heat-producing elements compared with the rest of the planet, then core heat fluxes
1378 might be somewhat higher there due to the cooler mantle temperatures. The relatively limited
1379 amount of lateral mixing of the mantle expected under low-Rayleigh-number convection,
1380 coupled with the small scale of convection, could act to preserve such heterogeneity.

1381 It is worth noting that MESSENGER gravity and topography data indicate that the domical
1382 rise within the northern volcanic plains is substantively compensated within ~100 km of the
1383 CMB (James *et al*., 2015). James *et al*. (2015) investigated a variety of mechanisms for the
1384 source of this compensation, including relief along a compositional interface (e.g., between the
1385 silicate mantle and a possible solid FeS layer at the top of the core) as well as other density
1386 variations. Variations in the thickness of an FeS layer would also result in changes in the
1387 thermal conductivity profile above the liquid core, leading to lateral differences in heat flux. A
1388 variety of compositions or viscosities at that depth may also induce additional thermal
1389 heterogeneity, though the impact of such variations relative to the remainder of the planet
1390 remains to be investigated.

1391 It is clear that heterogeneity within Mercury's mantle may influence the mechanisms by
1392 which the planet's magnetic field is generated, though more work – and the need for further
1393 observations – remains. Indeed, any geochemical and petrologic heterogeneity (Chapters 2, 7)
1394 inherited from Mercury's earliest history may have substantially influenced the planet's history
1395 yet, as less is known about the geochemical and geophysical character of the entire southern
1396 hemisphere than the north, we have much more to learn about the distribution of any
1397 heterogeneous properties of the interior.

1398 Mercury's internal structure and chemical make-up strongly influence the manner by which
1399 the planet's core, and therefore its magnetic field, has evolved. The discovery of Mercury's
1400 remanent crustal magnetism (Johnson *et al.*, 2015; Chapter 5) in crust that was last emplaced
1401 before ~3.7 Ga raises the question of how a planet cooling as modestly as suggested by its record
1402 of global contraction could have hosted both a relatively protracted period of early magnetic field
1403 generation and a modern field. A purely thermally generated dynamo that spans both time
1404 periods is unlikely, as the thermal history models indicate that core heat flux drops below the
1405 critical value for convection early in the planet's history and remains so. Indeed, early-onset
1406 thermal dynamos would tend to be short-lived, as evidenced by Figure 19.7 and previous
1407 modeling efforts (Hauck *et al.*, 2004; Grott *et al.*, 2011; Tosi *et al.*, 2013). Although much
1408 shorter than the upper bound of ~800 Myr implied by the surface age of the crust in areas of
1409 remanent magnetism, such shorter-duration dynamos are potentially consistent with
1410 observations, as the column of crust hosting the remanence may pre-date the surface age.
1411 Models with longer-lived supercritical core heat fluxes are also possible. Under that scenario,
1412 the simplest explanation for the modern magnetic field is that it restarted comparatively recently
1413 as a result of the onset of core crystallization and perhaps even inner core growth. Alternatively,

core crystallization could have been operating throughout the past 3.7 Gyr in order to account for both the ancient and modern fields. This mechanism is possible, yet would likely result in solidification of a substantial fraction of the core and greater contraction of the planet than has been documented so far. A large inner core does not appear to be compatible with the planet's internal structure (Hauck *et al.*, 2013; Dumberry and Rivoldini, 2015; Peale *et al.*, 2016) nor with magnetic field generation, as compositional gradients imposed by top-down crystallization, coupled with a large inner core, may serve to stabilize the entire core against convection (Dumberry and Rivoldini, 2015; Rückriemen *et al.*, 2015). Thus, a full understanding of the operation and evolution of Mercury's magnetic field depends on characterizing the age distribution of remanent crustal magnetism and understanding how core evolution, including the effects of core chemistry, was coupled to mantle convection and cooling through time.

## 19.7 Conclusions

MESSENGER has been instrumental in unveiling key elements of the global evolution of Mercury. From firmly establishing the occurrence of volcanism and its distribution in space and time, to substantively resolving the long-standing paradox between predicted and observed values for Mercury's global contraction and cooling, MESSENGER has brought new insight to fundamental questions about the planet that stood for nearly four decades. In turn, and as with all new missions of discovery, MESSENGER has raised new questions about how Mercury has operated over its history. With Mercury's remarkably thin mantle, which is incapable of significantly homogenizing its chemical character by mantle convection, it is clear that chemical heterogeneity has played an important role in the planet's history. The weak, axially aligned, and northward offset geometry of the internally generated magnetic field may be a distinct

manifestation of internal heterogeneity. However, it is the discovery of Mercury's ancient magnetic field, recorded in the crustal rocks, that may hold some of the deepest clues to the planet's internal evolution.

## References


Anderson, B. J., Johnson, C. L., Korth, H., Purucker, M. E., Winslow, R. M., Slavin, J. A., Solomon, S. C., McNutt, R. L., Jr., Raines, J. M. and Zurbuchen, T. H. (2011). The global magnetic field of Mercury from MESSENGER orbital observations. *Science,* **333,** 1859–1862, doi:10.1126/science.1211001.

Anderson, B. J., Johnson, C. L., Korth, H., Winslow, R. M., Borovsky, J. E., Purucker, M. E., Slavin, J. A., Solomon, S. C., Zuber, M. T. and McNutt, R. L., Jr. (2012). Low-degree structure in Mercury's planetary magnetic field. *J. Geophys. Res.,* **117,** E00L12, doi:10.1029/2012je004159.

Anderson, J. D., Jurgens, R. F., Lau, E. L., Slade, M. A., III and Schubert, G. (1996). Shape and orientation of Mercury from radar ranging data. *Icarus,* **124,** 690–697, doi:10.1006/icar.1996.0242.

Banks, M. E., Xiao, Z., Watters, T. R., Strom, R. G., Braden, S. E., Chapman, C. R., Solomon, S. C., Klimczak, C. and Byrne, P. K. (2015). Duration of activity on lobate-scarp thrust faults on Mercury. *J. Geophys. Res. Planets*, **120**, 1751–1762, doi:10.1002/2015je004828.

Berthet, S., Malavergne, V. and Righter, K. (2009). Melting of the Indarch meteorite (EH4 chondrite) at 1 GPa and variable oxygen fugacity: Implications for early planetary differentiation processes. *Geochim. Cosmochim. Acta,* **73,** 6402–6420, doi:10.1016/j.gca.2009.07.030.

Beuthe, M. (2010). East-west faults due to planetary contraction. *Icarus,* **209,** 795–817, doi:10.1016/j.icarus.2010.04.019.

1464

1465 Blair, D. M., Freed, A. M., Byrne, P. K., Klimczak, C., Prockter, L. M., Ernst, C. M., Solomon,
1466 S. C., Melosh, H. J. and Zuber, M. T. (2013). The origin of graben and ridges in
1467 Rachmaninoff, Raditladi, and Mozart basins, Mercury. *J. Geophys. Res. Planets,* **118,**
1468 47–58, doi:10.1029/2012JE004198.

1469 Breuer, D., Hauck, S. A., II, Buske, M., Pauer, M. and Spohn, T. (2007). Interior evolution of
1470 Mercury. *Space Sci. Rev.,* **132,** 229–260, doi:10.1007/s11214-007-9228-9.

1471 Brown, S. M. and Elkins-Tanton, L. T. (2009). Compositions of Mercury's earliest crust from
1472 magma ocean models. *Earth Planet. Sci. Lett.,* **286,** 446–455,
1473 doi:10.1016/j.epsl.2009.07.010.

1474 Bullard, E. and Gellman, H. (1954). Homogeneous dynamos and terrestrial magnetism. *Phil.*
1475 *Trans. Roy. Soc. Lond. A,* **247,** 213–278, doi:10.1098/rsta.1954.0018.

1476 Burbine, T. H., McCoy, T. J., Nittler, L. R., Benedix, G. K., Cloutis, E. A. and Dickinson, T. L.
1477 (2002). Spectra of extremely reduced assemblages: implications for Mercury. *Meteorit.*
1478 *Planet. Sci.,* **37,** 1233–1244, doi:10.1111/j.1945-5100.2002.tb00892.x.

1479 Byrne, P. K., Klimczak, C., Williams, D. A., Hurwitz, D. M., Solomon, S. C., Head, J. W.,
1480 Preusker, F. and Oberst, J. (2013). An assemblage of lava flow features on Mercury. *J.*
1481 *Geophys. Res. Planets,* **118,** 1303–1322, doi:10.1002/jgre.20052.

1482 Byrne, P. K., Klimczak, C., Şengör, A. M. C., Solomon, S. C., Watters, T. R. and Hauck, S. A.,
1483 II (2014). Mercury's global contraction much greater than earlier estimates. *Nature*
1484 *Geosci.,* **7,** 301–307, doi:10.1038/ngeo2097.

1485 Byrne, P. K., Ostrach, L. R., Fassett, C. I., Chapman, C. R., Denevi, B, W., Evans, A. J.,
1486 Klimczak, C., Banks, M. E., Head, J. W. and Solomon, S. C. (2016). Widespread effusive

volcanism on Mercury likely ended by about 3.5 Ga. *Geophys. Res. Lett.,* **43,** 7408–7416, doi:10.1002/2016GL069412.

Cao, H., Aurnou, J. M., Wicht, J., Dietrich, W., Soderlund, K. M. and Russell, C. T. (2014). A dynamo explanation for Mercury's anomalous magnetic field. *Geophys. Res. Lett.,* **41**, 4127–4134, doi:10.1002/2014gl060196.

Chabot, N. L., Wollack, E. A., Klima, R. L. and Minitti, M. E. (2014). Experimental constraints on Mercury's core composition. *Earth Planet. Sci. Lett.,* **390,** 199–208, doi:10.1016/j.epsl.2014.01.004.

Charlier, B., Grove, T. L. and Zuber, M. T. (2013). Phase equilibria of ultramafic compositions on Mercury and the origin of the compositional dichotomy. *Earth Planet. Sci. Lett.,* **363,** 50–60, doi:10.1016/j.epsl.2012.12.021.

Chen, B., Li, J. and Hauck, S. A., II (2008). Non-ideal liquidus curve in the Fe-S system and Mercury's snowing core. *Geophys. Res. Lett.,* **35,** L07201, doi:10.1029/2008gl033311.

Christensen, U. R. (2006). A deep dynamo generating Mercury's magnetic field. *Nature,* **444,** 1056–1058, doi:10.1038/nature05342.

Christensen, U. R. and Wicht, J. (2008). Models of magnetic field generation in partly stable planetary cores: Applications to Mercury and Saturn. *Icarus,* **196,** 16–34, doi:10.1016/j.icarus.2008.02.013.

Chudinovskikh, L. and Boehler, R. (2007). Eutectic melting in the system Fe–S to 44 GPa. *Earth Planet. Sci. Lett.,* **257,** 97–103, doi:10.1016/j.epsl.2007.02.024.

Correia, A. C. M. and Laskar, J. (2004). Mercury's capture into the 3/2 spin-orbit resonance as a result of its chaotic dynamics. *Nature,* **429,** 848–850, doi:10.1038/nature02609.

1509 Dasgupta, R., Buono, A., Whelan, G. and Walker, D. (2009). High-pressure melting relations in
1510 Fe–C–S systems: Implications for formation, evolution, and structure of metallic cores in
1511 planetary bodies. *Geochim. Cosmochim. Acta,* **73,** 6678–6691,
1512 doi:10.1016/j.gca.2009.08.001.
1513 de Koker, N., Steinle-Neumann, G. and Vlcek, V. (2012). Electrical resistivity and thermal
1514 conductivity of liquid Fe alloys at high P and T, and heat flux in Earth's core. *Proc. Nat.*
1515 *Acad. Sci.,* **109,** 4070-4073, doi:10.1073/pnas.1111841109.
1516 Denevi, B. W., Robinson, M. S., Solomon, S. C., Murchie, S. L., Blewett, D. T., Domingue, D.
1517 L., McCoy, T. J., Ernst, C. M., Head, J. W., Watters, T. R. and Chabot, N. L. (2009). The
1518 evolution of Mercury's crust: A global perspective from MESSENGER. *Science,* **324,**
1519 613–618, doi:10.1126/science.1172226.
1520 Denevi, B. W., Ernst, C. M., Meyer, H. M., Robinson, M. S., Murchie, S. L., Whitten, J. L.,
1521 Head, J. W., Watters, T. R., Solomon, S. C., Ostrach, L. R., Chapman, C. R., Byrne, P.
1522 K., Klimczak, C. and Peplowski, P. N. (2013a). The distribution and origin of smooth
1523 plains on Mercury. *J. Geophys. Res. Planets,* **118,** 891–907, doi:10.1002/jgre.20075.
1524 Denevi, B. W., Ernst, C. M., Whitten, J. L., Head, J. W., Murchie, S. L., Watters, T. R., Byrne,
1525 P. K., Blewett, D. T., Solomon, S. C. and Fassett, C. I. (2013b). The volcanic origin of a
1526 region of intercrater plains on Mercury. *Lunar Planet. Sci.*, **44**, abstract 1218.
1527 Deng, L., Fei, Y., Liu, X., Gong, Z. and Shahar, A. (2013a). Effect of carbon, sulfur and silicon
1528 on iron melting at high pressure: Implications for composition and evolution of the
1529 planetary terrestrial cores. *Geochim. Cosmochim. Acta,* **114,** 220–233,
1530 doi:10.1016/j.gca.2013.01.023.

1531 Deng, L., Seagle, C., Fei, Y. and Shahar, A. (2013b). High pressure and temperature electrical
1532 resistivity of iron and implications for planetary cores. *Geophys. Res. Lett.,* **40,** 33–37,
1533 doi:10.1029/2012GL054347.
1534 Di Achille, G., Popa, C., Massironi, M., Epifani, E. M., Zusi, M., Cremonese, G. and Palumbo,
1535 P. (2012). Mercury's radius change estimates revisited using MESSENGER data. *Icarus,*
1536 **221,** 456–460.
1537 Dombard, A. and Hauck, S. A., II (2008). Despinning plus global contraction and the orientation
1538 of lobate scarps on Mercury: Predictions for MESSENGER. *Icarus,* **198,** 274–276,
1539 doi:10.1016/j.icarus.2008.06.008.
1540 Dumberry, M. and Rivoldini, A. (2015). Mercury's inner core size and core-crystallization
1541 regime. *Icarus,* **248,** 254–268, doi:10.1016/j.icarus.2014.10.038.
1542 Egea-González, I., Ruiz, J., Fernández, C., Williams, J.-P., Márquez, Á. and Lara, L. M. (2012).
1543 Depth of faulting and ancient heat flows in the Kuiper region of Mercury from lobate
1544 scarp topography. *Planet. Space Sci.,* **60,** 193–198, doi:10.1016/j.pss.2011.08.003.
1545 Ernst, C. M., Murchie, S. L., Barnouin, O. S., Robinson, M. S., Denevi, B. W., Blewett, D. T.,
1546 Head, J. W., Izenberg, N. R., Solomon, S. C. and Roberts, J. H. (2010). Exposure of
1547 spectrally distinct material by impact craters on Mercury: Implications for global
1548 stratigraphy. *Icarus,* **209,** 210–223, doi:10.1016/j.icarus.2010.05.022.
1549 Ernst, C. M., Denevi, B. W., Barnouin, O. S., Klimczak, C., Chabot, N. L., Head, J. W.,
1550 Murchie, S. L., Neumann, G. A., Prockter, L. M., Robinson, M. S., Solomon, S. C. and
1551 Watters, T. R. (2015). Stratigraphy of the Caloris basin, Mercury: Implications for
1552 volcanic history and basin impact melt. *Icarus,* **250,** 413–429,
1553 doi:10.1016/j.icarus.2014.11.003.

1554 Evans, L. G., Peplowski, P. N., Rhodes, E. A., Lawrence, D. J., McCoy, T. J., Nittler, L. R.,
1555 Solomon, S. C., Sprague, A. L., Stockstill-Cahill, K. R., Starr, R. D., Weider, S. Z.,
1556 Boynton, W. V., Hamara, D. K. and Goldsten, J. O. (2012). Major-element abundances
1557 on the surface of Mercury: Results from the MESSENGER Gamma-Ray Spectrometer. *J.*
1558 *Geophys. Res.*, **117**, E00L07, doi:10.1029/2012je004178.
1559 Evans, L. G., P. N. Peplowski, F. M. McCubbin, T. J. McCoy, L. R. Nittler, M. Y. Zolotov, D. S.
1560 Ebel, D. J. Lawrence, R. D. Starr, S. Z. Weider, S. C. Solomon (2015). Chlorine on the
1561 surface of Mercury: MESSENGER gamma-ray measurements and implications for the
1562 planet's formation and evolution. *Icarus*, **257**, 417–427,
1563 doi:10.1016/j.icarus.2015.04.039.
1564 Fassett, C. I., Head, J. W., Blewett, D. T., Chapman, C. R., Dickson, J. L., Murchie, S. L.,
1565 Solomon, S. C. and Watters, T. R. (2009). Caloris impact basin: Exterior geomorphology,
1566 stratigraphy, morphometry, radial sculpture, and smooth plains deposits. *Earth Planet.*
1567 *Sci. Lett.,* **285,** 297–308, doi:10.1016/j.epsl.2009.05.022.
1568 Fassett, C. I., Kadish, S. J., Head, J. W., Solomon, S. C. and Strom, R. G. (2011). The global
1569 population of large craters on Mercury and comparison with the Moon. *Geophys. Res.*
1570 *Lett.,* **38,** L10202, doi:10.1029/2011gl047294.
1571 Fei, Y., Bertka, C. M. and Finger, L. W. (1997). High-pressure iron sulfur compound, $Fe_3S_2$, and
1572 melting relations in the Fe-FeS system. *Science,* **275,** 1621–1623,
1573 doi:10.1126/science.275.5306.1621.
1574 Fei, Y., Li, J., Bertka, C. M. and Prewitt, C. T. (2000). Structure type and bulk modulus of $Fe_3S$,
1575 a new iron-sulfur compound. *Am. Mineral.,* **85,** 1830–1833, doi:10.2138/am-2000-11-
1576 1229.

1577 Fei, Y., Hillgren, V. J., Shahar, A. and Solomon, S. C. (2011). On the silicon content of
1578 Mercury's core and implications for core mineralogy, structure, and density. *Lunar*
1579 *Planet. Sci.*, **42**, abstract 1949.
1580 Ferrari, S., Massironi, M., Marchi, S., Byrne, P. K., Klimczak, C., Martellato, E. and Cremonese,
1581 G. (2014). Age relationships of the Rembrandt basin and Enterprise Rupes, Mercury. In
1582 *Volcanism and Tectonism Across the Solar System*, ed. T. Platz, M. Massironi, P. K. Byrne
1583 and H. Hiesinger, Spec. Publ., **401**. London, United Kingdom: Geological Society, pp.
1584 159–172, doi:10.1144/SP401.20.
1585 Fischer, R. A., Campbell, A. J., Reaman, D. M., Miller, N. A., Heinz, D. L., Dera, P. and
1586 Prakapenka, V. B. (2013). Phase relations in the Fe–FeSi system at high pressures and
1587 temperatures. *Earth Planet. Sci. Lett.,* **373,** 54–64, doi:10.1016/j.epsl.2013.04.035.
1588 Freed, A. M., Solomon, S. C., Watters, T. R., Phillips, R. J. and Zuber, M. T. (2009). Could
1589 Pantheon Fossae be the result of the Apollodorus crater-forming impact within the
1590 Caloris basin, Mercury? *Earth Planet. Sci. Lett.,* **285,** 320–327,
1591 doi:10.1016/j.epsl.2009.02.038.
1592 Freed, A. M., Blair, D. M., Watters, T. R., Klimczak, C., Byrne, P. K., Solomon, S. C., Zuber,
1593 M. T. and Melosh, H. J. (2012). On the origin of graben and ridges within and near
1594 volcanically buried craters and basins in Mercury's northern plains. *J. Geophys. Res.,*
1595 **117,** E00L06, doi:10.1029/2012je004119.
1596 Glassmeier, K.-H., Auster, H.-U. and Motschmann, U. (2007). A feedback dynamo generating
1597 Mercury's magnetic field. *Geophys. Res. Lett.,* **34,** L22201, doi:10.1029/2007gl031662.

1598 Gomi, H., Ohta, K., Hirose, K., Labrosse, S., Caracas, R., Verstraete, M. J. and Hernlund, J. W.
1599 (2013). The high conductivity of iron and thermal evolution of the Earth's core. *Phys.*
1600 *Earth Planet. Inter.,* **224,** 88–103, doi:10.1016/j.pepi.2013.07.010.
1601 Goudge, T. A., Head, J. W., Kerber, L., Blewett, D. T., Denevi, B. W., Domingue, D. L., Gillis-
1602 Davis, J. J., Gwinner, K., Helbert, J., Holsclaw, G. M., Izenberg, N. R., Klima, R. L.,
1603 McClintock, W. E., Murchie, S. L., Neumann, G. A., Smith, D. E., Strom, R. G., Xiao,
1604 Zhiyong, Zuber, M. T., Solomon, S. C. (2014). Global inventory and characterization of
1605 pyroclastic deposits on Mercury: New insights into pyroclastic activity from
1606 MESSENGER orbital data, *J. Geophys. Res. Planets*, **119**, 635–658,
1607 doi:10.1002/2013JE004480.
1608 Grasset, O. and Parmentier, E. M. (1998). Thermal convection in a volumetrically heated,
1609 infinite Prandtl number fluid with strongly temperature-dependent viscosity: Implications
1610 for planetary thermal evolution. *J. Geophys. Res.,* **103,** 18171–18181,
1611 doi:10.1029/98JB01492.
1612 Grott, M., Breuer, D. and Laneuville, M. (2011). Thermo-chemical evolution and global
1613 contraction of Mercury. *Earth Planet. Sci. Lett.,* **307,** 135–146,
1614 doi:10.1016/j.epsl.2011.04.040.
1615 Hauck, S. A., II and Phillips, R. J. (2002). Thermal and crustal evolution of Mars. *J. Geophys.*
1616 *Res.,* **107,** 5052, doi:5010.1029/2001JE001801.
1617 Hauck, S. A., II, Dombard, A. J., Phillips, R. J. and Solomon, S. C. (2004). Internal and tectonic
1618 evolution of Mercury. *Earth Planet. Sci. Lett.,* **222,** 713–728,
1619 doi:10.1016/j.epsl.2004.03.037.

1620 Hauck, S. A., II, Aurnou, J. M. and Dombard, A. J. (2006). Sulfur's impact on core evolution and
1621 magnetic field generation on Ganymede. *J. Geophys. Res.,* **111,** E09008,
1622 doi:10.1029/2005je002557.
1623 Hauck, S. A., II, Margot, J.-L., Solomon, S. C., Phillips, R. J., Johnson, C. L., Lemoine, F. G.,
1624 Mazarico, E., McCoy, T. J., Padovan, S., Peale, S. J., Perry, M. E., Smith, D. E. and
1625 Zuber, M. T. (2013). The curious case of Mercury's internal structure. *J. Geophys. Res.*
1626 *Planets,* **118,** 1204-1220, doi:10.1002/jgre.20091.
1627 Head, J. W., Murchie, S. L., Prockter, L. M., Robinson, M. S., Solomon, S. C., Strom, R. G.,
1628 Chapman, C. R., Watters, T. R., McClintock, W. E., Blewett, D. T. and Gillis-Davis, J. J.
1629 (2008). Volcanism on Mercury: Evidence from the first MESSENGER Flyby. *Science,*
1630 **321,** 69–72, doi:10.1126/science.1159256.
1631 Head, J. W., Chapman, C. R., Strom, R. G., Fassett, C. I., Denevi, B. W., Blewett, D. T., Ernst,
1632 C. M., Watters, T. R., Solomon, S. C., Murchie, S. L., Prockter, L. M., Chabot, N. L.,
1633 Gillis-Davis, J. J., Whitten, J. L., Goudge, T. A., Baker, D. M. H., Hurwitz, D. M.,
1634 Ostrach, L. R., Xiao, Z., Merline, W. J., Kerber, L., Dickson, J. L., Oberst, J., Byrne, P.
1635 K., Klimczak, C. and Nittler, L. R. (2011). Flood Volcanism in the northern high latitudes
1636 of Mercury revealed by MESSENGER. *Science,* **333,** 1853–1856,
1637 doi:10.1126/science.1211997.
1638 Heimpel, M. H., Aurnou, J. M., Al-Shamali, F. M. and Gomez Perez, N. (2005). A numerical
1639 study of dynamo action as a function of spherical shell geometry. *Earth Planet. Sci. Lett.,*
1640 **236,** 542–557, doi:10.1016/j.epsl.2005.04.032.

1641 Herzberg, C. T., Raterron, P. and Zhang, J. (2000). New experimental observations on the
1642 anhydrous solidus for peridotite KLB-1. *Geophys. Geochem. Geosyst.,* **1,**
1643 doi:10.1029/2000GC000089.
1644 Heyner, D., Wicht, J., Gómez-Pérez, N., Schmitt, D., Auster, H.-U. and Glassmeier, K.-H.
1645 (2011). Evidence from numerical experiments for a feedback dynamo generating
1646 Mercury's magnetic field. *Science,* **334,** 1690–1693, doi:10.1126/science.1207290.
1647 Hurwitz, D. M., Head, J. W., Byrne, P. K., Xiao, Z., Solomon, S. C., Zuber, M. T., Smith, D. E.
1648 and Neumann, G. A. (2013). Investigating the origin of candidate lava channels on
1649 Mercury with MESSENGER data: Theory and observations. *J. Geophys. Res. Planets,*
1650 **118,** 471–486, doi:10.1029/2012je004103.
1651 James, P. B., Zuber, M. T., Phillips, R. J. and Solomon, S. C. (2015). Support of long-
1652 wavelength topography on Mercury inferred from MESSENGER measurements of
1653 gravity and topography. *J. Geophys. Res. Planets,* **120,** 287–310,
1654 doi:10.1002/2014je004713.
1655 Jing, Z., Wang, Y., Kono, Y., Yu, T., Sakamaki, T., Park, C., Rivers, M. L., Sutton, S. R. and
1656 Shen, G. (2014). Sound velocity of Fe–S liquids at high pressure: Implications for the
1657 Moon's molten outer core. *Earth Planet. Sci. Lett.,* **396,** 78–87,
1658 doi:10.1016/j.epsl.2014.04.015.
1659 Johnson, C. L., Phillips, R. J., Purucker, M. E., Anderson, B. J., Byrne, P. K., Denevi, B. W.,
1660 Feinberg, J. M., Hauck, S. A., Head, J. W., Korth, H., James, P. B., Mazarico, E.,
1661 Neumann, G. A., Philpott, L. C., Siegler, M. A., Tsyganenko, N. A. and Solomon, S. C.
1662 (2015). Low-altitude magnetic field measurements by MESSENGER reveal Mercury's
1663 ancient crustal field. *Science,* **348,** 892–895, doi:10.1126/science.aaa8720.

1664 Johnson, C. L., L. C. Philpott, B. J. Anderson, H. Korth, S. A. Hauck, II, D. Heyner, R. J.
1665 Phillips, R. M. Winslow, and S. C. Solomon (2016), MESSENGER observations of
1666 induced magnetic fields in Mercury's core, *Geophys. Res. Lett.*, **43**, 2436–2444,
1667 doi:10.1002/2015GL067370.
1668 Kaula, W. M. (1975). The seven ages of a planet. *Icarus,* **26,** 1–15, doi:10.1016/0019-
1669 1035(75)90138-4.
1670 Keil, K. (1989). Enstatite meteorites and their parent bodies. *Meteoritics,* **24,** 195–208.
1671 Kennedy, P. J., Freed, A. M. and Solomon, S. C. (2008). Mechanisms of faulting in and around
1672 Caloris basin, Mercury. *J. Geophys. Res.,* **113,** E08004, doi:10.1029/2007JE002992.
1673 Kerber, L., Head, J. W., Solomon, S. C., Murchie, S. L., Blewett, D. T. and Wilson, L. (2009).
1674 Explosive volcanic eruptions on Mercury: Eruption conditions, magma volatile content,
1675 and implications for interior volatile abundances. *Earth Planet. Sci. Lett.,* **285,** 263–271,
1676 doi:10.1016/j.epsl.2009.04.037.
1677 Kerber, L., Head, J. W., Blewett, D. T., Solomon, S. C., Wilson, L., Murchie, S. L., Robinson,
1678 M. S., Denevi, B. W. and Domingue, D. L. (2011). The global distribution of pyroclastic
1679 deposits on Mercury: The view from MESSENGER flybys 1-3. *Planet. Space Sci.,* **59,**
1680 1895–1909, doi:10.1016/j.pss.2011.03.020.
1681 King, S. D. (2008). Pattern of lobate scarps on Mercury's surface reproduced by a model of
1682 mantle convection. *Nature Geosci.,* **1,** 229–232, doi:10.1038/ngeo152.
1683 Kirk, R. L. and Stevenson, D. J. (1989). The competition between thermal contraction and
1684 differentiation in the stress history of the Moon. *J. Geophys. Res.,* **94,** 12133–12144,
1685 doi:10.1029/JB094iB09p12133.

1686 Klima, R. L., Blewett, D. T., Denevi, B. W. Ernst, C. M., Frank, E. A., Head, J. W., III, Izenberg,
1687 N. R., Murchie, S. L., Nittler, L. R., Peplowski, P. N. and Solomon, S. C. (2016). Global
1688 distribution and spectral properties of low-reflectance material on Mercury. *Lunar Planet.*
1689 *Sci.*, **47**, abstract 1195.
1690 Klimczak, C. (2015). Limits on the brittle strength of planetary lithospheres undergoing global
1691 contraction. *J. Geophys. Res. Planets*, **120**, 2135–2151, doi:10.1002/2015je004851.
1692 Klimczak, C., Watters, T. R., Ernst, C. M., Freed, A. M., Byrne, P. K., Solomon, S. C., Blair, D.
1693 M. and Head, J. W. (2012). Deformation associated with ghost craters and basins in
1694 volcanic smooth plains on Mercury: Strain analysis and implications for plains evolution.
1695 *J. Geophys. Res.,* **117,** E00L03, doi:10.1029/2012je004100.
1696 Knibbe, J. S. and van Westrenen, W. (2015). The interior configuration of planet Mercury
1697 constrained by moment of inertia and planetary contraction. *J. Geophys. Res. Planets,*
1698 **120,** 1904–1923, doi:10.1002/2015JE004908.
1699 Konôpková, Z., McWilliams, R. S., Gómez-Pérez, N. and Goncharov, A. F. (2016). Direct
1700 measurement of thermal conductivity in solid iron at planetary core conditions. *Nature*,
1701 **534**, 99–101, doi:10.1038/nature18009.
1702 Kuwayama, Y. and Hirose, K. (2004). Phase relations in the system Fe-FeSi at 21 GPa. *Am.*
1703 *Mineral.,* **89,** 273–276, doi:10.2138/am-2004-2-303.
1704 Le Feuvre, M. and Wieczorek, M. A. (2011). Nonuniform cratering of the Moon and a revised
1705 crater chronology of the inner Solar System. *Icarus,* **214,** 1–20,
1706 doi:10.1016/j.icarus.2011.03.010.
1707 Li, J., Fei, Y., Mao, H. K., Hirose, K. and Shieh, S. R. (2001). Sulfur in the Earth's inner core.
1708 *Earth Planet. Sci. Lett.,* **193,** 509–514, doi:10.1016/S0012-821X(01)00521-0.

1709 Lord, O. T., Walter, M. J., Dasgupta, R., Walker, D. and Clark, S. M. (2009). Melting in the Fe–
1710 C system to 70 GPa. *Earth Planet. Sci. Lett.,* **284,** 157–167,
1711 doi:10.1016/j.epsl.2009.04.017.
1712 Malavergne, V., Toplis, M. J., Berthet, S. and Jones, J. (2010). Highly reducing conditions
1713 during core formation on Mercury: Implications for internal structure and the origin of a
1714 magnetic field. *Icarus,* **206,** 199–209, doi:10.1016/j.icarus.2009.09.001.
1715 Manglik, A., Wicht, J. and Christensen, U. R. (2010). A dynamo model with double diffusive
1716 convection for Mercury's core. *Earth Planet. Sci. Lett.,* **289,** 619–628,
1717 doi:10.1016/j.epsl.2009.12.007.
1718 Marchi, S., Mottola, S., Cremonese, G., Massironi, M. and Martellato, E. (2009). A new
1719 chronology for the Moon and Mercury. *Astron. J.,* **137,** 4936–4948, doi:10.1088/0004-
1720 6256/137/6/4936.
1721 Marchi, S., Massironi, M., Cremonese, G., Martellato, E., Giacomini, L. and Prockter, L. (2011).
1722 The effects of the target material properties and layering on the crater chronology: The
1723 case of Raditladi and Rachmaninoff basins on Mercury. *Planet. Space Sci.,* **59,** 1968–
1724 1980, doi:10.1016/j.pss.2011.06.007.
1725 Marchi, S., Chapman, C. R., Fassett, C. I., Head, J. W., Bottke, W. F. and Strom, R. G. (2013).
1726 Global resurfacing of Mercury 4.0–4.1 billion years ago by heavy bombardment and
1727 volcanism. *Nature,* **499,** 59–61, doi:10.1038/nature12280.
1728 Margot, J. L., Peale, S. J., Jurgens, R. F., Slade, M. A. and Holin, I. V. (2007). Large longitude
1729 libration of Mercury reveals a molten core. *Science,* **316,** 710–714,
1730 doi:10.1126/science.1140514.

1731 Margot, J.-L., Peale, S. J., Solomon, S. C., Hauck, S. A., II, Ghigo, F. D., Jurgens, R. F.,
1732 Padovan, S. and Campbell, D. B. (2012). Mercury's moment of inertia from spin and
1733 gravity data. *J. Geophys. Res.,* **117,** E00L09, doi:10.1029/2012JE004161.
1734 Martin, A. M., Van Orman, J., Hauck, S. A., Chen, B., Sun, N., Moore, R. D. and Han, J. (2014).
1735 In situ determination of the eutectic melting temperature of Fe-FeS-Fe3C between 4.5
1736 and 24.5 GPa and implications for Mercury's core. *Lunar Planet. Sci.,* **45,** abstract 2854.
1737 Martin, A. M., Van Orman, J., Hauck, S. A., Sun, N., Yu, T. and Wang, Y. (2015). Role of
1738 sulfur, silicon and carbon on the crystallization processes in Mercury's core inferred from
1739 in-situ melting experiments between 4.5 and 15.5 GPa. *Lunar Planet. Sci.,* **46,** abstract
1740 2627.
1741 Matsuyama, I. and Nimmo, F. (2009). Gravity and tectonic patterns of Mercury: Effect of tidal
1742 deformation, spin-orbit resonance, nonzero eccentricity, despinning, and reorientation. *J.*
1743 *Geophys. Res.,* **114,** E01010, doi:10.1029/2008je003252.
1744 Mazarico, E., Genova, A., Goossens, S., Lemoine, F. G., Neumann, G. A., Zuber, M. T., Smith,
1745 D. E. and Solomon, S. C. (2014). The gravity field, orientation, and ephemeris of
1746 Mercury from MESSENGER observations after three years in orbit. *J. Geophys. Res.*
1747 *Planets,* **119,** 2417–2436, doi:10.1002/2014je004675.
1748 McCoy, T. J., Dickinson, T. L. and Lofgren, G. E. (1999). Partial melting of the Indarch (EH4)
1749 meteorite: A textural, chemical, and phase relations view of melting and melt migration.
1750 *Meteorit. Planet. Sci.,* **34,** 735–746, doi:10.1111/j.1945-5100.1999.tb01386.x.
1751 McCubbin, F. M., Riner, M. A., Vander Kaaden, K. E. and Burkemper, L. K. (2012). Is Mercury
1752 a volatile-rich planet? *Geophys. Res. Lett.,* **39,** L09202, doi:10.1029/2012gl051711.

1753 Melosh, H. J. (1977). Global tectonics of a despun planet. *Icarus,* **31,** 221–243, doi:
1754 10.1016/0019-1035(77)90035-5.
1755 Melosh, H. J. and Dzurisin, D. (1978). Mercurian global tectonics: A consequence of tidal
1756 despinning? *Icarus,* **35,** 227–236, doi:10.1016/0019-1035(78)90007-6.
1757 Melosh, H. J. and McKinnon, W. B. (1988). The tectonics of Mercury. In *Mercury*, ed. F. Vilas,
1758 C. R. Chapman and M. S. Matthews. Tucson, AZ: University of Arizona Press, pp. 374–
1759 400.
1760 Michel, N. C., Hauck, S. A., II, Solomon, S. C., Phillips, R. J., Roberts, J. H. and Zuber, M. T.
1761 (2013). Thermal evolution of Mercury as constrained by MESSENGER observations. *J.*
1762 *Geophys. Res. Planets,* **118,** 1033–1044, doi:10.1002/jgre.20049.
1763 Morard, G. and Katsura, T. (2010). Pressure–temperature cartography of Fe–S–Si immiscible
1764 system. *Geochim. Cosmochim. Acta,* **74,** 3659–3667, doi:10.1016/j.gca.2010.03.025.
1765 Morard, G., Andrault, D., Guignot, N., Siebert, J., Garbarino, G. and Antonangeli, D. (2011).
1766 Melting of Fe–Ni–Si and Fe–Ni–S alloys at megabar pressures: Implications for the core–
1767 mantle boundary temperature. *Phys. Chem. Minerals,* **38,** 767–776, doi:10.1007/s00269-
1768 011-0449-9.
1769 Moresi, L. N. and Solomatov, V. S. (1995). Numerical investigation of 2D convection with
1770 extremely large viscosity variations. *Phys. Fluids,* **7,** 2154–2162, doi: 10.1063/1.868465.
1771 Murchie, S. L., Watters, T. R., Robinson, M. S., Head, J. W., Strom, R. G., Chapman, C. R.,
1772 Solomon, S. C., McClintock, W. E., Prockter, L. M., Domingue, D. L. and Blewett, D. T.
1773 (2008). Geology of the Caloris basin, Mercury: A view from MESSENGER. *Science,*
1774 **321,** 73–76, doi:10.1126/science.1159261.

1775 Murchie, S. L., Klima, R. L., Denevi, B. W., Ernst, C. M., Keller, M. R., Domingue, D. L.,
1776 Blewett, D. T., Chabot, N. L., Hash, C. D., Malaret, E., Izenberg, N. R., Vilas, F., Nittler,
1777 L. R., Gillis-Davis, J. J., Head, J. W. and Solomon, S. C. (2015). Orbital multispectral
1778 mapping of Mercury with the MESSENGER Mercury Dual Imaging System: Evidence
1779 for the origins of plains units and low-reflectance material. *Icarus,* **254,** 287–305,
1780 doi:10.1016/j.icarus.2015.03.027.
1781 Murray, B. C., Belton, M. J. S., Danielson, G. E., Davies, M. E., Gault, D. E., Hapke, B.,
1782 O'Leary, B., Strom, R. G., Suomi, V. and Trask, N. (1974). Mercury's surface:
1783 Preliminary description and interpretation from Mariner 10 pictures. *Science,* **185,** 169–
1784 179.
1785 Murray, B. C., Strom, R. G., Trask, N. J. and Gault, D. E. (1975). Surface history of Mercury:
1786 Implications for terrestrial planets. *J. Geophys. Res.,* **80,** 2508–2514,
1787 doi:10.1029/JB080i017p02508.
1788 Namur, O. and Charlier, B. (2017). Silicate mineralogy at the surface of Mercury. *Nature*
1789 *Geosci*., **10**, 9–13, doi:10.1038/ngeo2860.
1790 Namur, O., M. Collinet, B. Charlier, T. L. Grove, F. Holtz, C. McCammon (2016). Melting
1791 processes and mantle sources of lavas on Mercury, *Earth Planet. Sci. Lett.*, **439**, 117–128,
1792 doi: 10.1016/j.epsl.2016.01.030.
1793 Ness, N. F. (1979). The magnetic field of Mercury. *Phys. Earth Planet. Inter.,* **20,** 209–217, doi:
1794 10.1016/0031-9201(79)90044-X.
1795 Ness, N. F., Behannon, K. W., Lepping, R. P. and Whang, Y. C. (1975). The magnetic field of
1796 Mercury. I. *J. Geophys. Res.,* **80,** 2708–2716, doi:10.1029/JA080i019p02708.

1797 Ness, N. F., Behannon, K. W., Lepping, R. P. and Whang, Y. C. (1976). Observations of
1798 Mercury's magnetic field. *Icarus,* **28,** 479–488, doi:10.1016/0019-1035(76)90121-4.
1799 Neukum, G., Ivanov, B. A. and Hartmann, W. K. (2001). Cratering records in the inner solar
1800 system in relation to the lunar reference system. *Space Sci. Rev.,* **96,** 55–86.
1801 Nimmo, F. and Stevenson, D. J. (2001). Estimates of Martian crustal thickness from viscous
1802 relaxation of topography. *J. Geophys. Res.,* **106,** 5085–5098, doi:10.1029/2000JE001331.
1803 Nittler, L. R., Starr, R. D., Weider, S. Z., McCoy, T. J., Boynton, W. V., Ebel, D. S., Ernst, C.
1804 M., Evans, L. G., Goldsten, J. O., Hamara, D. K., Lawrence, D. J., McNutt, R. L.,
1805 Schlemm, C. E., Solomon, S. C. and Sprague, A. L. (2011). The major-element
1806 composition of Mercury's surface from MESSENGER X-ray spectrometry. *Science,* **333,**
1807 1847–1850, doi:10.1126/science.1211567.
1808 Noyelles, B., Frouard, J., Makarov, V. V. and Efroimsky, M. (2014). Spin-orbit evolution of
1809 Mercury revisited. *Icarus,* **241,** 26–44, doi:10.1016/j.icarus.2014.05.045.
1810 Ostrach, L. R., Robinson, M. S., Whitten, J. L., Fassett, C. I., Strom, R. G., Head, J. W. and
1811 Solomon, S. C. (2015). Extent, age, and resurfacing history of the northern smooth plains
1812 on Mercury from MESSENGER observations. *Icarus,* **250,** 602–622,
1813 doi:10.1016/j.icarus.2014.11.010.
1814 Padovan, S., Margot, J.-L., Hauck, S. A., Moore, W. B. and Solomon, S. C. (2014). The tides of
1815 Mercury and possible implications for its interior structure. *J. Geophys. Res. Planets,*
1816 **119,** 850–866, doi:10.1002/2013je004459.
1817 Padovan, S., Wieczorek, M. A., Margot, J.-L., Tosi, N. and Solomon, S. C. (2015). Thickness of
1818 the crust of Mercury from geoid-to-topography ratios. *Geophys. Res. Lett.,* **42,** 1029–
1819 1038, doi:10.1002/2014gl062487.

1820 Peale, S. J. (1988). The rotational dynamics of Mercury and the state of its core. In *Mercury*, ed.
1821 F. Vilas, C. R. Chapman and M. S. Matthews. Tucson, AZ: University of Arizona Press,
1822 pp. 461–493.
1823 Peale, S. J., Phillips, R. J., Solomon, S. C., Smith, D. E. and Zuber, M. T. (2002). A procedure
1824 for determining the nature of Mercury's core. *Meteorit. Planet. Sci.,* **37,** 1269–1283,
1825 doi:10.1111/j.1945-5100.2002.tb00895.x.
1826 Peale, S. J., Margot, J.-L., Hauck, S. A., II and Solomon, S. C. (2016). Consequences of a solid
1827 inner core on Mercury's spin configuration. *Icarus,* **264,** 443–455,
1828 doi:10.1016/j.icarus.2015.09.024.
1829 Peplowski, P. N., Evans, L. G., Hauck, S. A., II, McCoy, T. J., Boynton, W. V., Gillis-Davis, J.
1830 J., Ebel, D. S., Goldsten, J. O., Hamara, D. K., Lawrence, D. J., McNutt, R. L., Nittler, L.
1831 R., Solomon, S. C., Rhodes, E. A., Sprague, A. L., Starr, R. D. and Stockstill-Cahill, K.
1832 R. (2011). Radioactive elements on Mercury's surface from MESSENGER: Implications
1833 for the planet's formation and evolution. *Science,* **333,** 1850–1852,
1834 doi:10.1126/science.1211576.
1835 Peplowski, P. N., Lawrence, D. J., Rhodes, E. A., Sprague, A. L., McCoy, T. J., Denevi, B. W.,
1836 Evans, L. G., Head, J. W., Nittler, L. R., Solomon, S. C., Stockstill-Cahill, K. R. and
1837 Weider, S. Z. (2012). Variations in the abundances of potassium and thorium on the
1838 surface of Mercury: Results from the MESSENGER Gamma-Ray Spectrometer. *J.*
1839 *Geophys. Res.,* **117,** E00L04, doi:10.1029/2012JE004141.
1840 Peplowski, P. N., Lawrence, D. J., Evans, L. G., Klima, R. L., Blewett, D. T., Goldsten, J. O.,
1841 Murchie, S. L., McCoy, T. J., Nittler, L. R., Solomon, S. C., Starr, R. D. and Weider, S.
1842 Z. (2015a). Constraints on the abundance of carbon in near-surface materials on Mercury:

Results from the MESSENGER Gamma-Ray Spectrometer. *Planet. Space Sci.,* **108,** 98–107, doi:10.1016/j.pss.2015.01.008.

Peplowski, P. N., Lawrence, D. J., Feldman, W. C., Goldsten, J. O., Bazell, D., Evans, L. G., Head, J. W., Nittler, L. R., Solomon, S. C. and Weider, S. Z. (2015b). Geochemical terranes of Mercury's northern hemisphere as revealed by MESSENGER neutron measurements. *Icarus,* **253,** 346–363, doi:10.1016/j.icarus.2015.02.002.

Peplowski, P. N., R. L. Klima, D. J. Lawrence, C. M. Ernst, B. W. Denevi, E. A. Frank, J. O. Goldsten, S. L. Murchie, L. R. Nittler, and S. C. Solomon, (2016), Remote sensing evidence for an ancient carbon-bearing crust on Mercury, *Nature Geosci.*, **9**, 273–276, doi:10.1038/ngeo2669.

Perry, M. E., Neumann, G. A., Phillips, R. J., Barnouin, O. S., Ernst, C. M., Kahan, D. S., Solomon, S. C., Zuber, M. T., Smith, D. E., Hauck, S. A., Peale, S. J., Margot, J.-L., Mazarico, E., Johnson, C. L., Gaskell, R. W., Roberts, J. H., McNutt, R. L., Jr. and Oberst, J. (2015). The low-degree shape of Mercury. *Geophys. Res. Lett.,* **42,** 6951–6958, doi:10.1002/2015gl065101.

Philpott, L. C., Johnson, C. L., Winslow, R. M., Anderson, B. J., Korth, H., Purucker, M. E. and Solomon, S. C. (2014). Constraints on the secular variation of Mercury's magnetic field from the combined analysis of MESSENGER and Mariner 10 data. *Geophys. Res. Lett.,* **41,** 6627–6634, doi:10.1002/2014gl061401.

Plesa, A. C., Tosi, N. and Hüttig, C. (2013). Thermo-chemical convection in planetary mantles: Advection methods and magma ocean overturn simulations. In *Integrated Information and Computing Systems for Natural, Spatial, and Social Sciences*, ed. R. Claus-Peter. Hershey, PA: IGI Global, pp. 302–323, doi:10.4018/978-1-4666-2190-9.ch015.

1866 Pozzo, M., Davies, C., Gubbins, D. and Alfe, D. (2012). Thermal and electrical conductivity of
1867 iron at Earth's core conditions. *Nature,* **485,** 355–358, doi:10.1038/nature11031.
1868 Prockter, L. M., Ernst, C. M., Denevi, B. W., Chapman, C. R., Head, J. W., Fassett, C. I.,
1869 Merline, W. J., Solomon, S. C., Watters, T. R., Strom, R. G., Cremonese, G., Marchi, S.
1870 and Massironi, M. (2010). Evidence for young volcanism on Mercury from the third
1871 MESSENGER flyby. *Science*, **329**, 668–671, doi:10.1126/science.1188186.
1872 Raghavan, V. (1988). *Phase Diagrams of Ternary Iron Alloys, Part 2: Ternary Systems*
1873 *Containing Iron and Sulphur.* Calcutta: Indian Institute of Metals.
1874 Redmond, H. L. and King, S. D. (2007). Does mantle convection currently exist on Mercury?
1875 *Phys. Earth Planet. Inter.,* **164,** 221–231, doi:10.1016/j.pepi.2007.07.004.
1876 Reese, C. C., Solomatov, V. S. and Moresi, L. N. (1998). Heat transport efficiency for stagnant
1877 lid convection with dislocation viscosity: Application to Venus and Mars. *J. Geophys.*
1878 *Res.,* **103,** 13643–13658, doi:10.1029/98JE01047.
1879 Riner, M. A., Lucey, P. G., Desch, S. J. and McCubbin, F. M. (2009). Nature of opaque
1880 components on Mercury: Insights into a Mercurian magma ocean. *Geophys. Res. Lett.,*
1881 **36,** L02201, doi:10.1029/2008GL036128.
1882 Rivera-Valentin, E. G. and Barr, A. C. (2014). Impact-induced compositional variations on
1883 Mercury. *Earth Planet. Sci. Lett.,* **391,** 234–242, doi:10.1016/j.epsl.2014.02.003.
1884 Rivoldini, A. and Van Hoolst, T. (2013). The interior structure of Mercury constrained by the
1885 low-degree gravity field and the rotation of Mercury. *Earth Planet. Sci. Lett.,* **377–378,**
1886 62–72, doi:10.1016/j.epsl.2013.07.021.

1887 Roberts, J. H. and Barnouin, O. S. (2012). The effect of the Caloris impact on the mantle
1888 dynamics and volcanism of Mercury. *J. Geophys. Res.,* **117,** E02007,
1889 doi:10.1029/2011JE003876.
1890 Robinson, M. S. and Lucey, P. G. (1997). Recalibrated Mariner 10 color mosaics: Implications
1891 for Mercurian volcanism. *Science,* **275,** 197–200, doi:10.1126/science.275.5297.197.
1892 Robinson, M. S., Murchie, S. L., Blewett, D. T., Domingue, D. L., Hawkins, S. E., Head, J. W.,
1893 Holsclaw, G. M., McClintock, W. E., McCoy, T. J., McNutt, R. L., Prockter, L. M.,
1894 Solomon, S. C. and Watters, T. R. (2008). Reflectance and color variations on Mercury:
1895 Regolith processes and compositional heterogeneity. *Science,* **321,** 66–69,
1896 doi:10.1126/science.1160080.
1897 Rückriemen, T., Breuer, D. and Spohn, T. (2015). The Fe snow regime in Ganymede's core: A
1898 deep-seated dynamo below a stable snow zone. *J. Geophys. Res. Planets,* **120,** 1095–
1899 1118, doi:10.1002/2014JE004781.
1900 Schubert, G., Ross, M. N., Stevenson, D. J. and Spohn, T. (1988). Mercury's thermal history and
1901 the generation of its magnetic field. In *Mercury*, ed. F. Vilas, C. R. Chapman and M. S.
1902 Matthews. Tucson, AZ: University of Arizona Press, pp. 429–460.
1903 Schumacher, S. and Breuer, D. (2006). Influence of a variable thermal conductivity on the
1904 thermochemical evolution of Mars. *J. Geophys. Res.*, **111**, E02006,
1905 doi:10.1029/2005JE002429.
1906 Seagle, C. T., Cottrell, E., Fei, Y., Hummer, D. R. and Prakapenka, V. B. (2013). Electrical and
1907 thermal transport properties of iron and iron-silicon alloy at high pressure. *Geophys. Res.*
1908 *Lett.,* **40,** 5377–5381, doi:10.1002/2013gl057930.

1909 Siegfried, R. W., II and Solomon, S. C. (1974). Mercury: Internal structure and thermal
1910 evolution. *Icarus,* **23,** 192–205, doi: 10.1016/0019-1035(74)90005-0.
1911 Smith, D. E., Zuber, M. T., Lemoine, F. G., Solomon, S. C., Hauck, S. A., II, Lemoine, F. G.,
1912 Mazarico, E., Phillips, R. J., Neumann, G. A., Peale, S. J., Margot, J.-L., Johnson, C. L.,
1913 Torrence, M. H., Perry, M. E., Rowlands, D. D., Goossens, S., Head, J. W. and Taylor, A.
1914 H. (2012). Gravity field and internal structure of Mercury from MESSENGER. *Science,*
1915 **336,** 214–217, doi:10.1126/science.1218809.
1916 Solomon, S. C. (1976). Some aspects of core formation in Mercury. *Icarus,* **28,** 509–521,
1917 doi:10.1016/0019-1035(76)90124-X.
1918 Solomon, S. C. (1977). The relationship between crustal tectonics and internal evolution in the
1919 Moon and Mercury. *Phys. Earth Planet. Inter.,* **15,** 135–145, doi:10.1016/0031-
1920 9201(77)90026-7.
1921 Solomon, S. C. (2003). Mercury: The enigmatic innermost planet. *Earth Planet. Sci. Lett.,* **216,**
1922 441–455, doi:10.1016/s0012-821x(03)00546-6.
1923 Spudis, P. D. and Guest, J. E. (1988). Stratigraphy and geologic history of Mercury. In *Mercury*,
1924 ed. F. Vilas, C. R. Chapman and M. S. Matthews. Tucson, AZ: University of Arizona
1925 Press, pp. 118–164.
1926 Stanley, S. and Bloxham, J. (2016). On the secular variation of Saturn's magnetic field. *Phys.*
1927 *Earth Planet. Inter.,* **250,** 31–34, doi:10.1016/j.pepi.2015.11.002.
1928 Stanley, S., Bloxham, J., Hutchison, W. and Zuber, M. (2005). Thin shell dynamo models
1929 consistent with Mercury's weak observed magnetic field. *Earth Planet. Sci. Lett.,* **234,**
1930 27–38, doi:10.1016/j.epsl.2005.02.040.

1931 Stevenson, D. J., Spohn, T. and Schubert, G. (1983). Magnetism and thermal evolution of the
1932 terrestrial planets. *Icarus,* **54,** 466–489, doi:10.1016/0019-1035(83)90241-5.
1933 Stewart, A. J., Schmidt, M. W., van Westrenen, W. and Liebske, C. (2007). Mars: A new core-
1934 crystallization regime. *Science,* **316,** 1323–1325, doi:10.1126/science.1140549.
1935 Stockstill-Cahill, K. R., McCoy, T. J., Nittler, L. R., Weider, S. Z. and Hauck, S. A., II (2012).
1936 Magnesium-rich crustal compositions on Mercury: Implications for magmatism from
1937 petrologic modeling. *J. Geophys. Res.,* **117,** E00L15, doi:10.1029/2012JE004140.
1938 Strom, R. G. (1977). Origin and relative age of lunar and Mercurian intercrater plains. *Phys.*
1939 *Earth Planet. Inter.,* **15,** 156–172, doi:10.1016/0031-9201(77)90028-0.
1940 Strom, R. G. and Neukum, G. (1988). The cratering record on Mercury and the origin of
1941 impacting objects. In *Mercury*, ed. F. Vilas, C. R. Chapman and M. S. Matthews. Tucson,
1942 AZ: University of Arizona Press, pp. 336–373.
1943 Strom, R. G., Trask, N. J. and Guest, J. E. (1975). Tectonism and volcanism on Mercury. *J.*
1944 *Geophys. Res.,* **80,** 2478–2507, doi:10.1029/JB080i017p02478.
1945 Strom, R. G., Chapman, C. R., Merline, W. J., Solomon, S. C. and Head, J. W. (2008). Mercury
1946 cratering record viewed from MESSENGER's first flyby. *Science,* **321,** 79–81, doi:
1947 10.1126/science.1159317.
1948 Strom, R. G., Banks, M. E., Chapman, C. R., Fassett, C. I., Forde, J. A., Head, J. W., III,
1949 Merline, W. J., Prockter, L. M. and Solomon, S. C. (2011). Mercury crater statistics from
1950 MESSENGER flybys: Implications for stratigraphy and resurfacing history. *Planet.*
1951 *Space Sci.,* **59,** 1960–1967, doi:10.1016/j.pss.2011.03.018.

1952 Taylor, G. J. and Scott, E. R. D. (2003). Mercury. In *Meteorites, Comets and Planets*, ed. A. M.
1953 Davis, vol. 1 of *Treatise on Geochemistry*, ed. H. D. Holland and K. K. Turekian. New
1954 York: Pergamon, pp. 477–485, doi:10.1016/B0-08-043751-6/01071-9.
1955 Thomas, R. J., Rothery, D. A., Conway, S. J. and Anand, M. (2014). Mechanisms of explosive
1956 volcanism on Mercury: Implications from its global distribution and morphology. *J.*
1957 *Geophys. Res. Planets,* **119,** 2239–2254, doi:10.1002/2014je004692.
1958 Tian, Z., Zuber, M. T. and Stanley, S. (2015). Magnetic field modeling for Mercury using
1959 dynamo models with a stable layer and laterally variable heat flux. *Icarus,* **260,** 263–268,
1960 doi:10.1016/j.icarus.2015.07.019.
1961 Tosi, N., Grott, M., Plesa, A. C. and Breuer, D. (2013). Thermochemical evolution of Mercury's
1962 interior. *J. Geophys. Res. Planets,* **118,** 2474–2487, doi:10.1002/jgre.20168.
1963 Tosi, N., Čadek, O., Běhounková, M., Káňová, M., Plesa, A. C., Grott, M., Breuer, D., Padovan,
1964 S. and Wieczorek, M. A. (2015). Mercury's low-degree geoid and topography controlled
1965 by insolation-driven elastic deformation. *Geophys. Res. Lett.,* **42,** 7327–7335,
1966 doi:10.1002/2015gl065314.
1967 Trask, N. J. and Guest, J. E. (1975). Preliminary geologic terrain map of Mercury. *J. Geophys.*
1968 *Res.,* **80,** 2461–2477, doi:10.1029/JB080i017p02461.
1969 Vander Kaaden, K. E. and McCubbin, F. M. (2015). Exotic crust formation on Mercury:
1970 Consequences of a shallow, FeO-poor mantle. *J. Geophys. Res. Planets,* **120,** 195–209,
1971 doi:10.1002/2014je004733.
1972 Vander Kaaden, K. E. and McCubbin, F. M. (2016). The origin of boninites on Mercury: An
1973 experimental study of the northern volcanic plains lavas. *Geochim. Cosmochim. Acta,*
1974 **173,** 246–263, doi:10.1016/j.gca.2015.10.016.

1975 Vasavada, A. R., Paige, D. A. and Wood, S. E. (1999). Near-surface temperatures on Mercury
1976 and the Moon and the stability of polar ice deposits. *Icarus,* **141,** 179–193,
1977 doi:10.1006/icar.1999.6175.
1978 Verma, A., and J.-L. Margot (2016). Mercury's gravity, tides, and spin from MESSENGER radio
1979 science data, *J. Geophys. Res. Planets*, **121**, 1627–1640, doi:10.1002/2016JE005037.
1980 Vilim, R., Stanley, S. and Hauck, S. A., II (2010). Iron snow zones as a mechanism for
1981 generating Mercury's weak observed magnetic field. *J. Geophys. Res.,* **115,** E11003,
1982 doi:10.1029/2009JE003528.
1983 Watters, T. R. and Nimmo, F. (2010). Tectonism on Mercury. In *Planetary Tectonics*, ed. T. R.
1984 Watters and R. A. Schultz. Cambridge: Cambridge University Press, pp. 15–80.
1985 Watters, T. R., Robinson, M. S. and Cook, A. C. (1998). Topography of lobate scarps on
1986 Mercury: New constraints on the planet's contraction. *Geology*, **26,** 991–994.
1987 Watters, T. R., Solomon, S. C., Robinson, M. S., Head, J. W., André, S. L., Hauck, S. A., II and
1988 Murchie, S. L. (2009). The tectonics of Mercury: The view after MESSENGER's first
1989 flyby. *Earth Planet. Sci. Lett.,* **285,** 283–296, doi:10.1016/j.epsl.2009.01.025.
1990 Watters, T. R., Selvans, M. M., Banks, M. E., Hauck, S. A., Becker, K. J. and Robinson, M. S.
1991 (2015a). Distribution of large-scale contractional tectonic landforms on Mercury:
1992 Implications for the origin of global stresses. *Geophys. Res. Lett.,* **42,** 3755–3763,
1993 doi:10.1002/2015gl063570.
1994 Watters, T. R., Solomon, S. C., Daud, K., Banks, M. E., Selvans, M. M., Robinson, M. S.,
1995 Murchie, S. L., Chabot, N. L., Denevi, B. W., Ernst, C. M., Chapman, C. R., Fassett, C.
1996 I., Klimczak, C., Byrne, P. K. and Blewett, D. T. (2015b). Small thrust fault scarps on

Mercury revealed in low-alitude MESSENGER images. *Lunar Planet. Sci.*, **46**, abstract 2240.

Weider, S. Z., Nittler, L. R., Starr, R. D., McCoy, T. J., Stockstill-Cahill, K. R., Byrne, P. K., Denevi, B. W., Head, J. W. and Solomon, S. C. (2012). Chemical heterogeneity on Mercury's surface revealed by the MESSENGER X-Ray Spectrometer. *J. Geophys. Res.,* **117,** E00L05, doi:10.1029/2012je004153.

Weider, S. Z., Nittler, L. R., Starr, R. D., Crapster-Pregont, E. J., Peplowski, P. N., Denevi, B. W., Head, J. W., Byrne, P. K., Hauck, S. A., II, Ebel, D. S. and Solomon, S. C. (2015). Evidence for geochemical terranes on Mercury: Global mapping of major elements with MESSENGER's X-Ray Spectrometer. *Earth Planet. Sci. Lett.,* **416,** 109–120, doi:10.1016/j.epsl.2015.01.023.

Whitten, J. L., Head, J. W., Denevi, B. W. and Solomon, S. C. (2014). Intercrater plains on Mercury: Insights into unit definition, characterization, and origin from MESSENGER datasets. *Icarus,* **241,** 97–113, doi:10.1016/j.icarus.2014.06.013.

Wicht, J. and Heyner, D. (2014). Mercury's magnetic field in the MESSENGER era. In *Planetary Geodesy and Remote Sensing*, ed. S. Jin. New York: CRC Press, pp. 223–262.

Wieczorek, M. A., Neumann, G. A., Nimmo, F., Kiefer, W. S., Taylor, G. J., Melosh, H. J., Phillips, R. J., Solomon, S. C., Andrews-Hanna, J. C., Asmar, S. W., Konopliv, A. S., Lemoine, F. G., Smith, D. E., Watkins, M. M., Williams, J. G. and Zuber, M. T. (2013). The crust of the Moon as seen by GRAIL. *Science,* **339,** 671–675, doi:10.1126/science.1231530.

2018 Williams, J.-P., Ruiz, J., Rosenburg, M. A., Aharonson, O. and Phillips, R. J. (2011). Insolation
2019 driven variations of Mercury's lithospheric strength. *J. Geophys. Res.,* **116,** E01008,
2020 doi:10.1029/2010JE003655.
2021 Williams, Q. (2009). Bottom-up versus top-down solidification of the cores of small solar system
2022 bodies: Constraints on paradoxical cores. *Earth Planet. Sci. Lett.,* **284,** 564–569,
2023 doi:10.1016/j.epsl.2009.05.019.
2024 Zhang, P., Cohen, R. E. and Haule, K. (2015). Effects of electron correlations on transport
2025 properties of iron at Earth's core conditions. *Nature,* **517,** 605–607,
2026 doi:10.1038/nature14090.
2027 Zolotov, M. Yu., Sprague, A. L., Hauck, S. A., Nittler, L. R., Solomon, S. C. and Weider, S. Z.
2028 (2013). The redox state, FeO content, and origin of sulfur-rich magmas on Mercury. *J.*
2029 *Geophys. Res. Planets,* **118,** 138–146, doi:10.1029/2012je004274.
2030

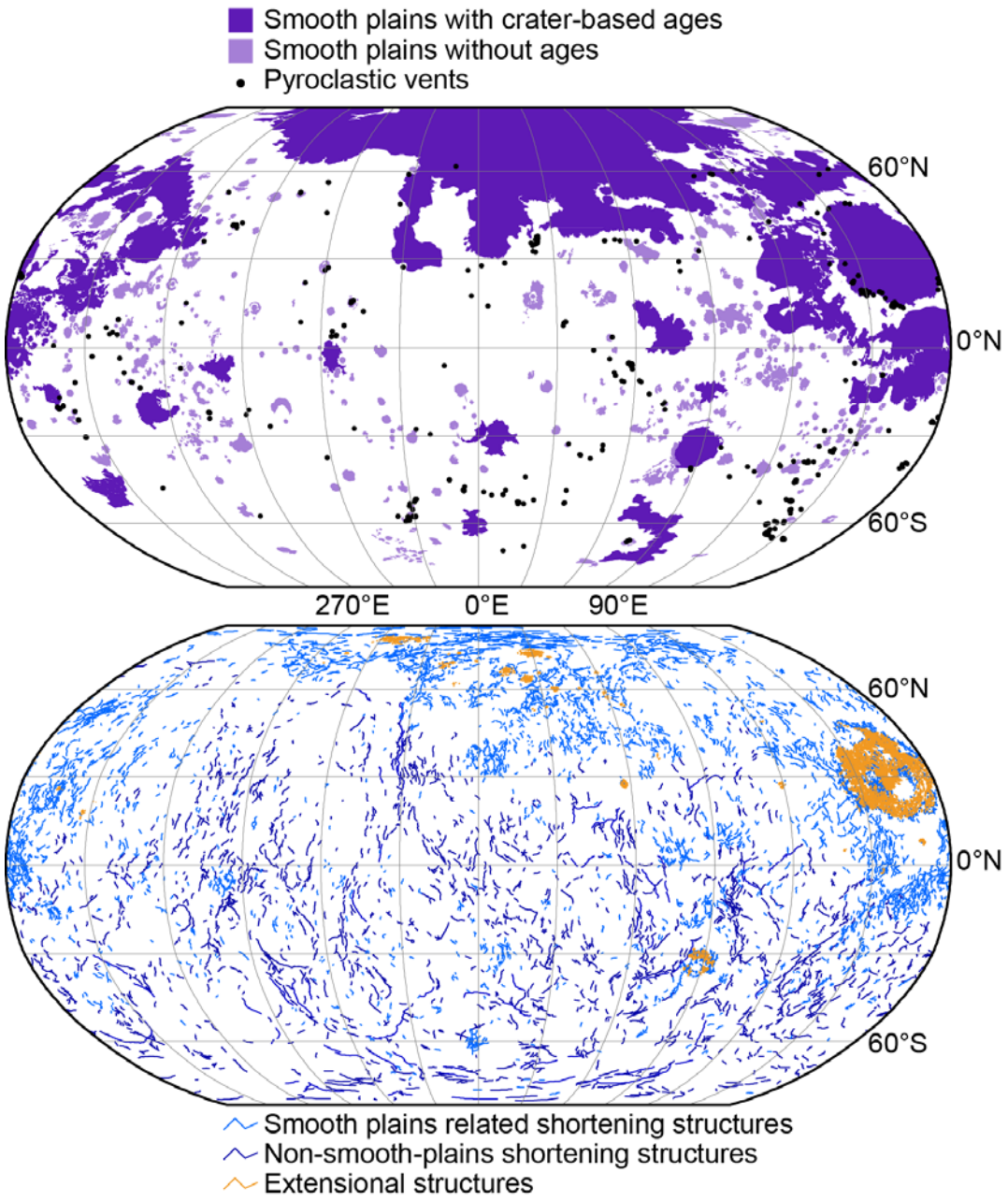


2031

2032

2033 Figure 19.1. Overview of major geological features on Mercury. Top: Smooth plains are in
2034 purple; the darker units have estimated ages whereas the lighter shade units are too small for
2035 reliable crater-based ages. Mapped units are from Denevi *et al.* (2013) and Byrne *et al.* (2016).
2036 Locations of pyroclastic vents are from the compilation of Thomas *et al.* (2014). Bottom:

2037 Compilation of tectonic structures, with shortening structures outlined in shades of blue and
2038 extensional structures in orange. Structures in the light blue are associated with smooth plains
2039 units as outlined in the top map in purple. The shortening structures are from Byrne *et al*.
2040 (2014), and the extensional structures are compiled from Klimczak *et al*. (2012), Ferrari *et al*.
2041 (2014), and Chapter 10.

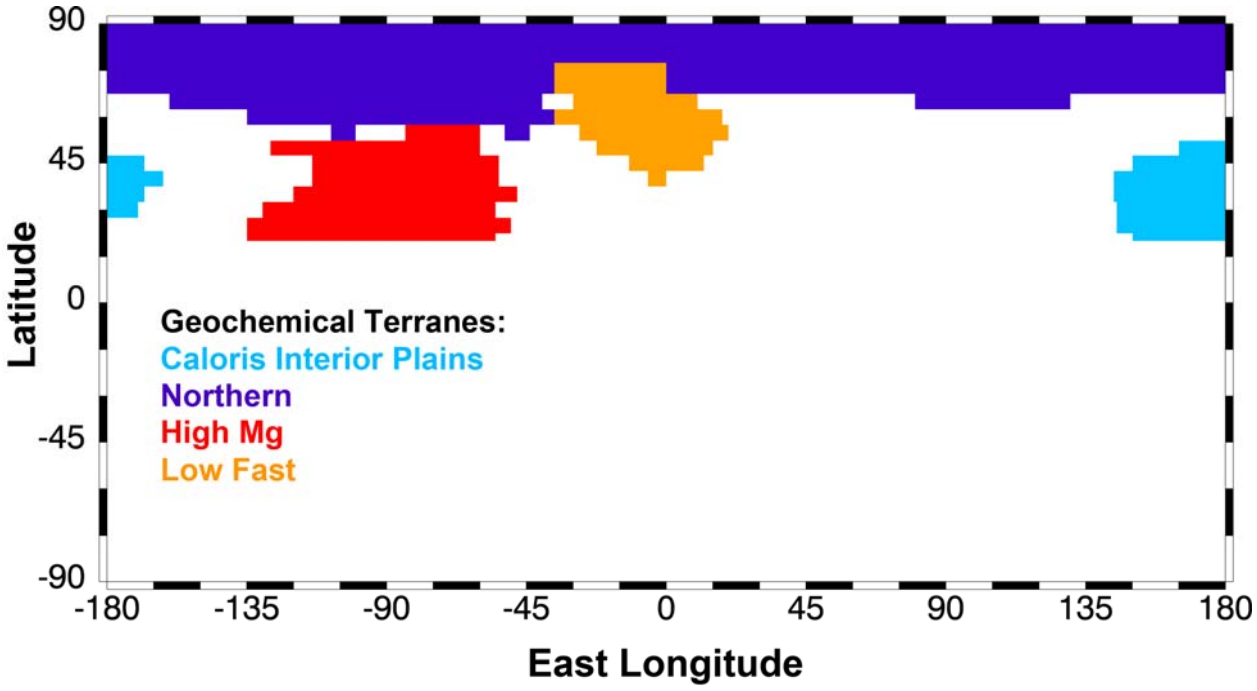


2042

2043 Figure 19.2. Overview of geochemically distinct terranes on Mercury (Chapters 2, 7). Figure
2044 from Patrick Peplowski.

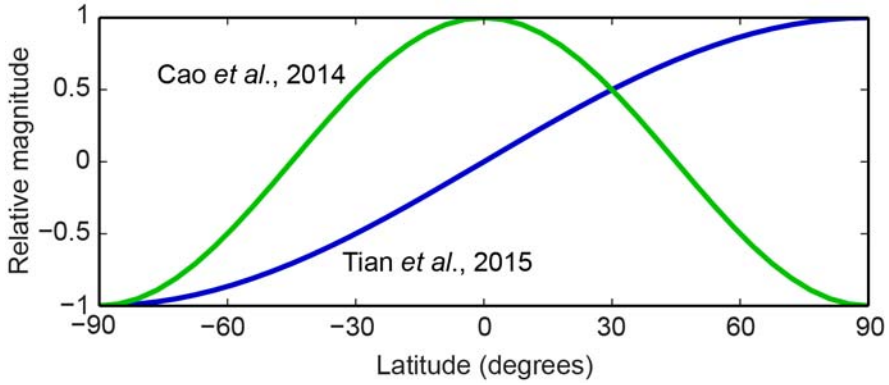


2045

Figure 19.3. Relative variations in the imposed heat flux along the core–mantle boundary in MESSENGER-era dynamo models. The work of Cao *et al*. (2014) invoked a core heat flux that is higher at, and symmetric about, the equator, whereas Tian *et al*. (2015) assumed a core heat flux that is greater in the northern hemisphere than in the southern hemisphere.

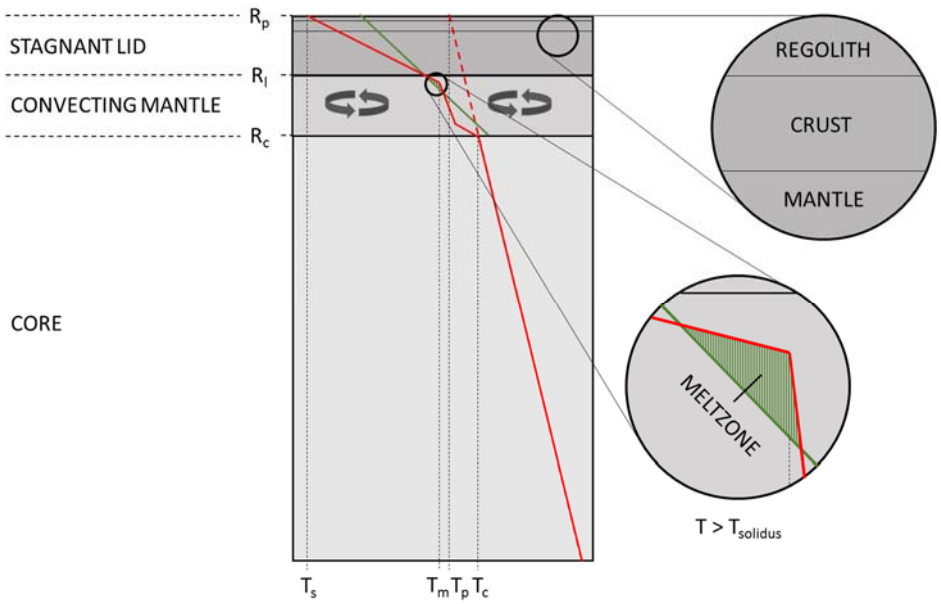


Figure 19.4 Schematic diagram of the reservoirs considered in parameterized thermal evolution models, including the stagnant lid, the convecting mantle, and the core. The planetary radius $R_p$, stagnant lid radius $R_l$, and core radius $R_c$ are indicated. Temperatures shown are the surface temperature $T_s$, the upper mantle temperature $T_m$, the mantle potential temperature $T_p$, and the core temperature $T_c$, with temperatures increasing to the right. The mantle solidus is indicated schematically by the green line, and the melt zone in which the local temperature exceeds the solidus is indicated by the filled area in the lower inset.

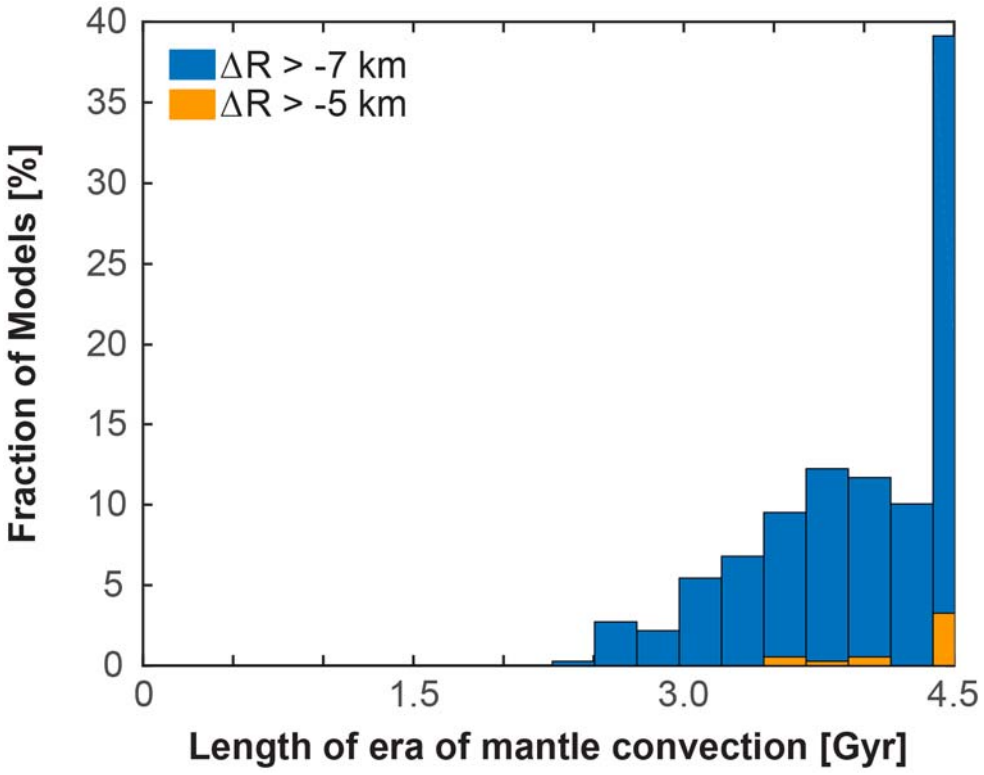


Figure 19.5. Results of Monte Carlo simulations of Mercury's thermal evolution for the duration of mantle convection. A total of 351 (blue) out of 2000 models from the simulations are consistent with the constraints posed by Mercury's magmatic evolution, global contraction, and magnetic field generation. The histogram shows the fraction of models in which mantle convection stopped at a given time. About 40% of the successful models convect to the present. Models shown in blue predict a reduction in planetary radius of between 5 to 7 km. This result should be compared with the models in orange, in which global contraction less than 5 km occurs but which otherwise satisfy the constraints, indicating the sensitivity of the inference on the longevity of mantle convection to the total observed radial contraction. Because of the uncertainty in core composition (section 19.4.4), contraction from inner core growth is neglected in these calculations. Note that the convention for global contraction here is a negative change in radius.

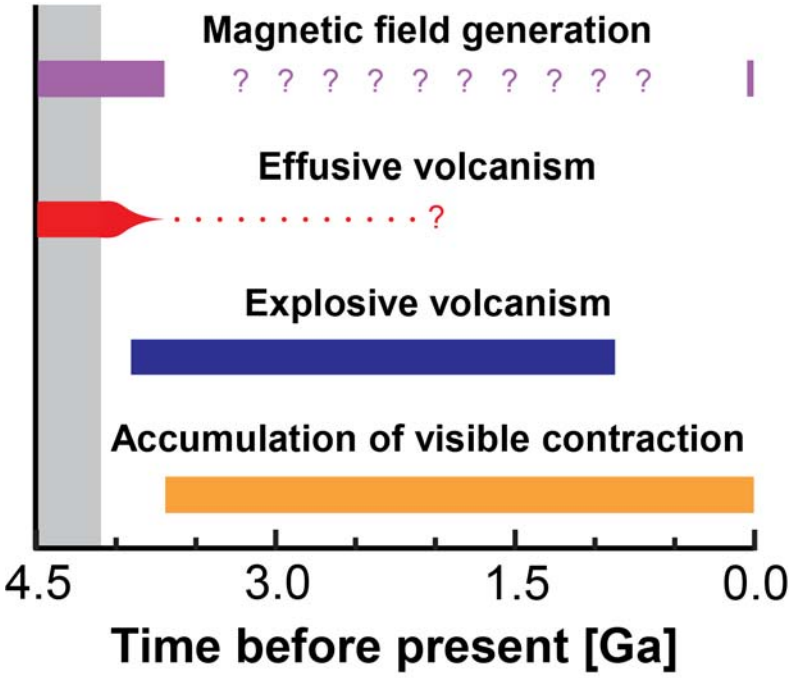


2071

2072 Figure 19.6. Schematic timeline of major processes in Mercury's evolution. Evidence of the
2073 planet's history during the first ~500 Myr has been erased by effusive volcanism and impact
2074 bombardment, as indicated by the gray shading.

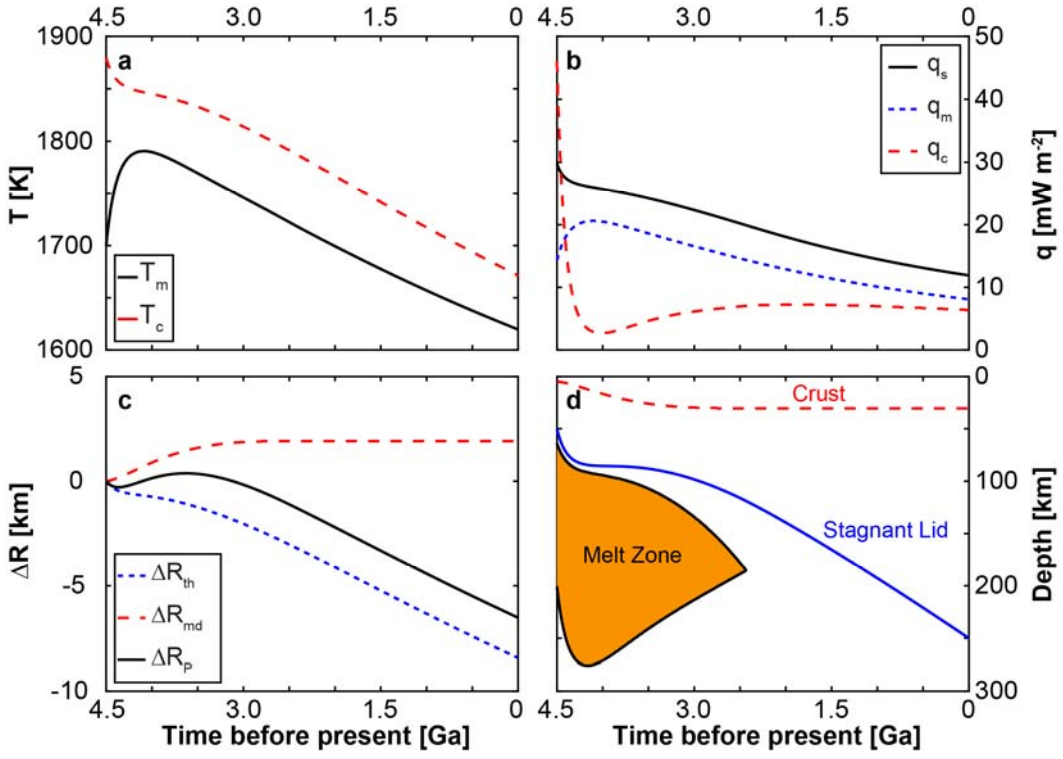


2075

Figure 19.7. Representative thermo-chemical evolution model for Mercury with parameters as discussed in the text. (a) Evolution of mantle temperature $T_m$ and CMB temperature $T_c$; (b) evolution of the surface heat flux $q_s$, mantle heat flux $q_m$, and core heat flux $q_c$; (c) evolution of the planetary radius change from thermal expansion and contraction of the mantle and core $R_{th}$, from mantle differentiation $R_{md}$, and of the sum of the two contributions $R_P$; (d) evolution of the thickness of the secondary crust, of the stagnant lid, and of the region in which partial melting occurs.

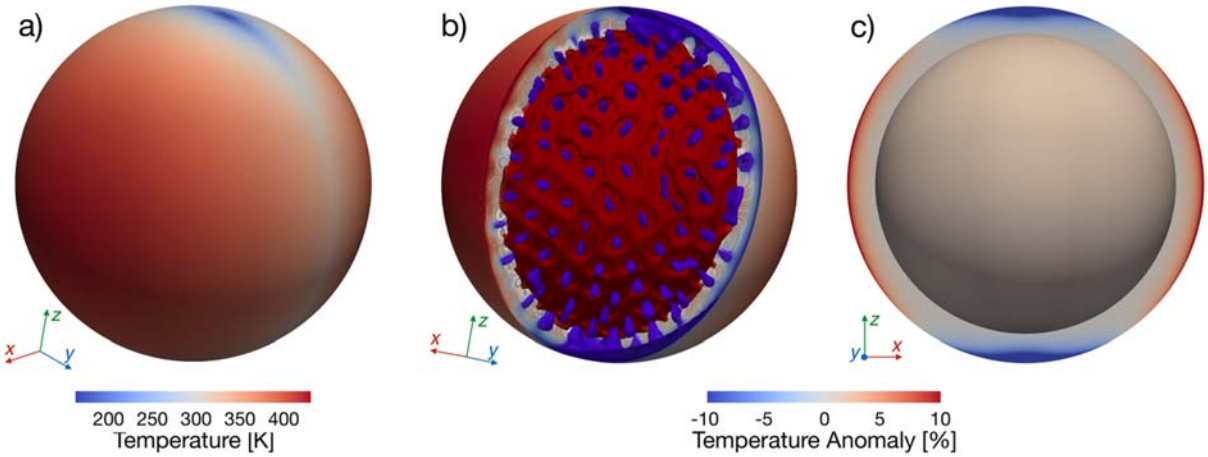


Figure 19.8. (a) Distribution of Mercury's average near-surface temperature according to the model of Vasavada *et al*. (1999). Hot equatorial poles are located at 0° and 180° E longitude, whereas cold poles are located at ±90° E. (b) Interior temperature anomalies after 1 Gyr of evolution when the mantle was still convecting. The color scale refers to the two mantle slices passing through the 0° and 90° meridional planes (the *x*–*z* and *y*–*z* planes, respectively), on top of which streamlines are plotted. Blue isovolumes mark the locations of downwelling that is 4 to 5% colder than average; red isovolumes refer to upwelling that is 1 to 2% hotter than average. (c) Interior temperature anomalies at present after the mantle transitioned to a conductive state, shown on the 0° meridional plane (*x*–*z*). Figure courtesy of Nicola Tosi.